Research Square

Preprints are preliminary reports that have not undergone peer review.
They should not be considered conclusive, used to inform clinical practice,
or referenced by the media as validated information.

Intensified atmosphere–sea ice coupling reshapes Arctic sea ice decline and downstream climate extremes

Shaoyin Wang

wangshy96@mail.sysu.edu.cn

Sun Yan-Sen University

Jiping Liu

Sun Yat-sen University

Zehao Wang

Sun Yat-sen University

Deliang Chen

Tsinghua University https://orcid.org/0000-0003-0288-5618

Peter Braesicke

Deutscher Wetterdienst https://orcid.org/0000-0003-1423-0619

Shengping He

Geophysical Institute, University of Bergen and Bjerknes Centre for Climate Research
https://orcid.org/0000-0003-4245-357X

Annette Rinke

https://orcid.org/0000-0002-6685-9219

Edward Hanna

University of Lincoln https://orcid.org/0000-0002-8683-182X

Jingfang Fan

Beijing Normal University https://orcid.org/0000-0003-1954-4641

Hua Li

Nanjing University of Information Science & Technology

Xiao Cheng

Sun Yan-sen University

Article

Keywords:

Posted Date: March 31st, 2026

DOI: https://doi.org/10.21203/rs.3.rs-9059403/v1

License: This work is licensed under a Creative Commons Attribution 4.0 International License.
Read Full License

Additional Declarations: There is **NO** Competing Interest.

Intensified atmosphere–sea ice coupling reshapes Arctic sea ice decline and downstream climate extremes

Shaoyin Wang[1, 2*], Jiping Liu[3,2*], Zehao Wang[1, 2], Deliang Chen[4], Peter Braesicke[5, a], Shengping He[6,11], Annette Rinke[7], Edward Hanna[8], Jingfang Fan[9], Hua Li[10], and Xiao Cheng[1, 2*]

[1]School of Geospatial Engineering and Science, Sun Yat-sen University, and Southern Marine Science and Engineering Guangdong Laboratory (Zhuhai), Zhuhai, China.

[2]Key Laboratory of Comprehensive Observation of Polar Environment (Sun Yat-sen University), China.

[3]School of Atmospheric Science, Sun Yat-sen University, and Southern Marine Science and Engineering Guangdong Laboratory (Zhuhai), Zhuhai, China.

[4]Department of Earth System Science, Tsinghua University, Beijing 100084, China.

[5]Institute of Meteorology and Climate Research Atmospheric Trace Gases and Remote Sensing (IMKASF), Karlsruhe Institute of Technology, Karlsruhe, Germany.

[6]Geophysical Institute, University of Bergen and Bjerknes Centre for Climate Research, Bergen, Norway.

[7]Alfred Wegener Institute, Helmholtz Centre for Polar and Marine Research, Potsdam, Germany.

[8]Department of Geography and Lincoln Climate Research Group, University of Lincoln, Lincoln, United Kingdom.

[9]School of Systems Science/Institute of Nonequilibrium Systems, Beijing Normal University, Beijing 100875, China.

[10]State Key Laboratory of Climate System Prediction and Risk Management/Key Laboratory of Hydrometeorological Disaster Mechanism and Warning of Ministry of Water Resources/Collaborative Innovation Center on Forecast and Evaluation of Meteorological Disasters, Nanjing University of Information Science & Technology, Nanjing, 210044, China.

[11]Nansen Environmental and Remote Sensing Center, Bergen, Norway.

[a]Now at: Business Area Research and Development, Deutscher Wetterdienst, Offenbach am Main, Germany.

Correpondance to:

wangshy96@mail.sysu.edu.cn; liujp63@mail.sysu.edu.cn; chengxiao9@mail.sysu.edu.cn

Abstract

Despite continued global warming and progressive thinning of Arctic sea ice, the rate of September sea ice decline has slowed markedly since the 2012 record low. This apparent stabilization challenges expectations of monotonic ice loss and remains poorly understood. Here we show that the slowdown reflects a regime shift in atmosphere–sea ice coupling, rather than a weakening of atmospheric influence. Around 2004, the relationship between the June Greenland High (GH) and September Arctic sea ice extent intensified dramatically, with the correlation strengthening from r = −0.17 (1979–2003) to r = −0.80 (2004–2025). This shift coincides with the transition to a thinner, younger, and more mobile ice cover that is more responsive to atmospheric forcing, alongside enhanced intra-seasonal persistence of summer Arctic circulation. Within this strengthened coupling regime, post-2012 GH weakening accounts for approximately 60–70% of the observed slowdown in September sea ice decline. Crucially, this apparent stabilization entails pronounced downstream impacts, including intensified marine heatwaves in the Norwegian–Barents Seas, accelerated rainfall transition in the Atlantic Arctic, and amplified summer heat extremes over northern Europe. Our findings demonstrate that atmosphere–sea ice coupling is non-stationary and has fundamentally strengthened in the New Arctic, amplifying the influence of circulation variability on both sea ice trajectories and midlatitude climate extremes, with important implications for prediction and climate projections.

Introduction

In response to global warming, Arctic sea ice extent (SIE) has declined in all seasons, with the most pronounced retreat occurring in summer[1,2]. Climate models project ice-free Arctic summers (commonly defined as SIE below 1 million km²) as early as the 2030s under moderate to high emission scenarios[3,4]. Concurrent with this decline, the Arctic sea ice cover has undergone a fundamental transformation: perennial multi-year ice (MYI) has been progressively replaced by thinner, more mobile first-year ice (FYI), ushering in a new and more vulnerable sea ice regime[5,6]. Thinner ice melts more rapidly under warm air advection[7] and enhanced oceanic heat flux from below[8,9], leading to reduced ice persistence and increasing sensitivity to external forcing[10,11]. Yet paradoxically, despite continued thinning and increasing vulnerability, the rate of September SIE decline has slowed markedly since the 2012 record low[12,13]. Explaining this apparent slowdown remains a central challenge in Arctic climate research.

The temporal evolution of sea ice extent, concentration, and thickness over decadal timescales (hereafter referred to as the "sea ice trajectory") is shaped not only by anthropogenic forcing but also by internal climate variability. Atmospheric circulation anomalies account for an estimated 40–50% of the observed summer sea ice loss during 1979–2014[7,14], primarily through intensified anticyclonic circulation that enhances lower-tropospheric warming, downward longwave radiation, and surface melt. Among these circulation features, the Greenland High (GH), a persistent summertime anticyclonic anomaly over Greenland closely linked to the North Atlantic Oscillation (NAO)[15], has emerged as a dominant driver of summer sea ice variability due to its strong influence on poleward heat and moisture transport, and wind-driven ice motion[16,17]. Clouds further modulate these processes: summertime low clouds mediate the impact of large-scale circulation on sea ice by regulating surface radiative fluxes in both shortwave and longwave bands[18,19], while winter and spring cloud anomalies precondition the ice for subsequent summer melt[20-22].

Several studies have proposed distinct mechanisms to explain the post-2012 slowdown. Ye et al. attributed the slowdown to accelerated North Pacific warming, which excites a Rossby wavetrain propagating into the Arctic and induces a downward trend in the summer Arctic Dipole (AD; the second EOF of Arctic SLP variability, with centres of action over the Canadian Arctic and Siberia), favouring sea ice retention in the central Arctic and Canadian Archipelago[23]. From an Atlantic perspective, Wang et al. linked the slowdown to multidecadal NAO variability, arguing that the transition from a negative to a positive NAO phase since the early 2010s has reduced poleward heat and moisture transport into the Arctic[24]. However, the NAO's influence on Arctic heat transport is regionally complex: positive NAO phases tend to reduce meridional heat transport, yet may enhance zonal flow and heat transport into the Atlantic Arctic sector. The Atlantic Multidecadal Oscillation (AMO) has also been implicated in modulating interdecadal variability of both the NAO and Arctic sea ice through wave–mean flow interactions[25,26]. While these studies highlight important teleconnection pathways, they largely assume stationary atmosphere–sea ice relationships and emphasize remote forcing mechanisms, offering limited insight into how local coupling dynamics (e.g., surface heat fluxes) may have fundamentally evolved alongside the changing sea ice state.

The focus on atmospheric modes of variability as possible drivers of change might overlook a critical question: has the sensitivity of Arctic sea ice to atmospheric forcing intensified as the sea ice cover has thinned and retreated? As sea ice retreats and becomes more seasonal, the overlying atmosphere responds through altered surface heat fluxes, moisture availability, and boundary layer stability, which can in turn feed back onto atmospheric circulation[27-29]. Both modelling experiments and observational analyses demonstrate that sea ice loss warms the Arctic boundary layer, weakens the meridional temperature gradient, and modifies transient eddy heat fluxes, with implications for the persistence and spatial structure of high-latitude circulation anomalies[30-32]. Interactions suggest that atmosphere–sea ice coupling should strengthen in a younger, thinner ice regime, with potentially profound consequences for both recent variability and future projections of Arctic sea ice loss.

Here, we investigate decadal changes in the relationship between the June GH and summer Arctic sea ice over the period 1979–2025. We identify a regime shift in GH–SIE coupling around 2004 through change point detection, which defines two primary analysis periods: Period 1 (P1: 1979–2003), representing the "Old Arctic" characterized by relatively weak atmosphere–sea ice coupling, and Period 2 (P2: 2004–2025), representing the "New Arctic" with substantially intensified coupling. Within P2, we further distinguish between 2004–2012, during which positive GH anomalies accelerated sea ice loss, and a weak GH phase (2013–2025), during which predominantly negative GH anomalies contributed to the observed slowdown. This framework separates the structural intensification of atmosphere–sea ice coupling (P1 to P2) from the subsequent reversal in circulation anomalies (strong to weak GH), clarifying how the same strengthened coupling can either accelerate or decelerate sea ice loss depending on the phase of atmospheric variability.

We address three key questions: (1) how has the GH–sea ice relationship evolved, and what is the evidence supports intensified coupling? (2) What physical mechanisms, particularly reduced ice persistence and enhanced atmospheric persistenc, underlie this intensification? And (3) what are the broader climatic consequences of the changing GH influence on regional and downstream climate extremes? By reframing the post-2012 slowdown not as a weakening of atmospheric forcing but as the outcome of intensified coupling to a weakening circulation pattern, we provide a new perspective on how evolving atmosphere–sea ice interactions shape both the Arctic sea ice trajectory and mid-latitude climate extremes.

Results

Post-2012 slowdown in Arctic sea ice decline and intensified GH–sea ice correlation

Over 1979–2025, September Arctic SIE declines at a rate of -0.76×10^6 km² per decade (-12.9% per decade). Mean September SIE decreases from $6.83 \pm 0.55 \times 10^6$ km² during Period 1 (P1, 1979–2003) to $4.79 \pm 0.57 \times 10^6$ km² during Period 2 (P2, 2004–2025), representing an overall reduction of 30% (**Fig. 1a**). The decades preceding 2012 are characterized by rapid ice loss, culminating in record-low extents in 2007 and 2012 (**Fig. 1a**). Since 2012, no new record low has been set. Consistent with the recent finding that Arctic sea ice loss has slowed considerably over the past two decades[13], a 20-year rolling trend analysis reveals that the rate of decline

peaked around 2012 (-1.47×10^6 km² per decade), with trends consistently significant ($p < 0.05$) throughout the early 2000s (**Fig. 1b**). Subsequently, however, the 20-year trend has progressively weakened as the rolling window increasingly incorporates the post-2012 period. The most recent 20-year trends (2005–2024 and 2006–2025) have diminished to −0.36 and -0.23×10^6 km² per decade, respectively, and neither is statistically significant, signifying a pronounced slowdown in summer Arctic sea ice decline.

This post-2012 slowdown exhibits distinct spatial characteristics relative to the earlier period of rapid sea ice decline (**Fig. 1c**). The Pacific Arctic sector (PAS), particularly over the northern Chukchi Sea, shows a reduced rate of sea ice loss relative to the preceding decades. By contrast, the Atlantic Arctic sector has continued to experience sea ice decline, most notably in the East Greenland Sea. After removing the long-term downward trend, sea ice concentration anomalies of +30–40% emerge over the PAS (**Fig. 1d**), indicating that sea ice loss in this region has proceeded more slowly than expected from the long-term trend. We emphasize that this signal reflects a deceleration of decline rather than a reversal or recovery of sea ice. Indeed, recent observations (for example, September 2025; **Extended Data Fig. 1**) confirm that sea ice coverage in the PAS remains relatively low. The emergence of this regional and basin-scale slowdown despite continued anthropogenic forcing and ongoing global warming underscores the critical role of internal climate variability in modulating the Arctic sea ice trajectory.

Among the key Arctic atmospheric circulations, the GH stands out as a dominant driver of summer sea ice changes (**Extended Data Fig. 2**). Over the full analysis period, the detrended correlation between June GH and September SIE is −0.50 ($p < 0.01$, $n = 47$). Correlations strengthen progressively from June through September (**Extended Data Fig. 2b, c**), consistent with the cumulative influence of atmospheric forcing over the summer melt season. Importantly, this relationship is non-stationary. Running correlation analysis of linearly detrended data reveals a clear transition around 2004: the June GH–September SIE correlation strengthens from $r = -0.17$ (not significant) during P1 to $r = -0.80$ during P2 ($p < 0.01$), a result that is robust across window lengths of 9–13 years (**Fig. 1e**). This abrupt intensification of the relationship is further confirmed by change point detection, which identifies 2004 as the most probable transition year ($p < 0.01$) using the PELT algorithm (see **Methods**). Transfer entropy analysis independently detects a regime shift around 2004–2006, confirming the strengthening of directional information flow from the atmosphere to sea ice (see **Supplementary Information**).

Notably, this transition is broadly consistent with the timing when the 20-year rolling SIE trend loses statistical significance (**Fig. 1b**), highlighting the importance of the intensified GH–SIE relationship for Arctic sea ice trajectory in the "New Arctic". A comparable intensification around 2004 is also evident in the June NAO– and AD–September SIE relationships (**Fig. S2a, c**), as well as the AO–SIE relationship (**Fig. S2b**). Consistent results are obtained using JJA-averaged circulation indices and both JJA and September sea ice extent (**Figs. S2 and S3**), all indicating a coherent strengthening of the atmosphere–sea ice relationships. As detailed in the following sections, this statistical intensification reflects a genuine enhancement of physical coupling: the transition to a thinner, more mobile ice cover increases the sensitivity of sea ice to atmospheric forcing, while enhanced intra-seasonal persistence of circulation anomalies

amplifies cumulative impacts over the melt season.

Evolution of the GH and its strengthening impacts on Arctic sea ice

We next examine the temporal evolution of the GH and its expanding spatial influence on Arctic sea ice. The June GH index exhibits pronounced interannual variability, with distinct multi-year phases evident over recent decades (**Fig. 2a**). Prior to 2000, the GH shows no clear trend. In contrast, persistent positive anomalies dominated during 2007–2012, followed by predominantly negative anomalies after 2012. This post-2012 GH weakening is evident in the broader spatial pattern of 500-hPa geopotential height (Z500) trends: strong positive trends over Greenland during the 2004–2012 transition to near-neutral or weakly negative trends when the analysis is extended to 2004–2025 (**Fig. 2b, c**). The post-2012 GH weakening coincides with a shift toward a more positive NAO phase (**Fig. 2a**). Using detrended regression analysis, we estimate that GH weakening explains approximately 70% of the ~1.1×10^6 km² increase in mean September SIE from the strong-GH phase (2007–2012) to the weak-GH phase (2013–2025) (see **Methods**).

The spatial imprint of June GH anomalies on sea ice concentration also differs markedly between the two periods (**Fig. 2d–g**). During P1, the GH influence is largely confined to the Beaufort Sea. During P2, this influence expands eastward across the Chukchi and East Siberian Seas, encompassing nearly the entire PAS. Notably, the spatial pattern of GH-related sea ice anomalies during P2 closely resembles the observed pattern of post-2012 sea ice retention in the PAS (**Fig. 1c vs. Fig. 2g**), indicating that the weakening of the GH after 2012 has played a substantial role in slowing regional sea ice loss.

The strengthened GH impact during P2 extends beyond sea ice concentration to include sea ice thickness and drift (**Fig. 2h–k**). GH weakening is associated with significant thickening across the PAS, with the affected area expanding from P1 to P2 (**Fig. 2h, i**). Conversely, over the North Atlantic sector, GH weakening corresponds to thinning north of Greenland, potentially threatening the Last Ice Area, where the thickest, oldest Arctic sea ice persists[33]. The GH influence on sea ice drift speed also intensifies during P2, expanding across the Chukchi and Beaufort Seas (**Fig. 2j, k**). These findings underscore that in the "New Arctic", sea ice has become increasingly responsive to atmospheric circulation anomalies, amplifying the GH influence on both the thermodynamic and dynamic components of the basin-wide sea ice mass balance.

Physical mechanisms: sea ice vulnerability and atmospheric persistence

Between P1 and P2, June-July-August-September (JJAS) sea ice thickness (SIT) declined by approximately 1 m across much of the Arctic Ocean, with the most pronounced reductions over the Canadian Basin, including the PAS (**Fig. 3a; Extended Data Fig. 3**). Mean sea ice age decreased from ~3 years to ~1 year, reflecting a large-scale transition from multi-year ice to first-year ice dominance (**Fig. 3a; Extended Data Fig. 3**). In parallel, sea ice mobility increased, as indicated by enhanced drift speeds, particularly over the Chukchi Sea (**Extended Data Fig. 3**). Together, these structural changes fundamentally altered sea ice persistence. During P1, summer SIT autocorrelation exceeded 0.8 across the Beaufort Sea and central

Arctic; during P2, autocorrelation values dropped below 0.6 over large parts of the PAS (**Fig. 3b–e**). The spatial pattern of reduced persistence closely follows the decline in ice thickness and age (**Extended Data Fig. 3**). Notably, these reductions in persistence over the PAS extend into the winter months (**Fig. 3f, g**). Physically, thinner and younger ice has lower thermal inertia, rendering it more responsive to atmospheric forcing and less capable of sustaining anomalies through the melt season.

In contrast to the declining persistence of the sea ice system, high-latitude atmospheric circulation has become more persistent. The intra-seasonal persistence of the GH increased substantially in P2 (**Extended Data Fig. 4**): the June–July GH correlation strengthened from 0.29 to 0.54, while the June–August correlation increased from 0.06 to 0.53 (**Extended Data Fig. 4a**). Notably, neither correlation is statistically significant during P1 ($p > 0.05$), whereas both become highly significant during P2 ($p < 0.01$). This enhanced persistence is confined to the summer months (June–August) and does not extend into September. Similar increases in persistence are evident for the NAO, Arctic Oscillation (AO), and AD patterns **(Extended Data Fig. 4b–d)**, indicating a broader regime shift toward more persistent summer Arctic circulation anomalies.

Consistent with this enhanced persistence, the spatial footprint of GH-related circulation anomalies expands markedly in P2. Regression analyses show that June GH anomalies during P2 generate stronger and more spatially extensive geopotential height anomalies that propagate into the central Arctic throughout JJAS (**Extended Data Fig. 5a–c**). These circulation responses are accompanied by increased total column water vapor (**Extended Data Fig. 5d–f)** and enhanced downward longwave radiation over the Atlantic Arctic sector **(Extended Data Fig. 6-7**). The surface energy budget response differs sharply between periods. During P2, regression magnitudes of net surface heat flux substantially exceed those of P1 across the Arctic marginal seas, indicating an amplified sensitivity of the surface energy budget to atmospheric circulation variability as the ice cover thins (**Fig. S4a, b**). By contrast, over the PAS, anomalous cyclonic circulation during weak GH conditions reduces meridional heat and moisture transport, limiting surface warming. Composite differences in net surface heat flux confirm reduced energy input over the Pacific Arctic during the weak GH phase, driven by diminished shortwave absorption under enhanced cloud cover and reduced turbulent heat exchange (**Fig. S4c**). As a result, post-2012 GH weakening has favoured relative cooling and sea ice retention in the PAS, while simultaneously promoting warming and continued sea ice loss in the Atlantic Arctic sector.

Together, declining sea ice persistence and increasing intra-seasonal atmospheric persistence amplify the cumulative seasonal impact of GH anomalies.

Downstream consequences: marine heatwaves, rainfall transition, and European heat extremes

Atmospheric circulation anomalies associated with GH variability also exert pronounced downstream impacts on ocean surface conditions and the high-latitude hydrological cycle. The post-2012 weakening of the GH coincides with a transition toward a more positive phase of

the June NAO (**Fig. 2a**), leading to fundamental changes in North Atlantic storm-track behaviour[34]. During the weak GH phase, enhanced cyclonic activity over the Atlantic Arctic sector increases the intensity of storms propagating into the Greenland and Barents Seas (**Extended Data Fig. 8a–c**). These circulation changes result in elevated precipitation over Svalbard and the East Greenland Sea (**Extended Data Fig. 8d–f; Fig. 4a, d**). Increased precipitation over eastern Greenland may partially mitigate regional ice-sheet mass loss through enhanced snowfall accumulation[35].

Enhanced cyclonic activity and strengthened poleward flow during the weak GH phase advect warm, moist air into the North Atlantic and Barents Sea, promoting more frequent and intense marine heatwaves (MHWs). Relative to the preceding strong GH phase (2007–2012), MHW intensity in the Norwegian–Barents Seas increased by more than 0.8°C during the weak GH phase (**Fig. 4b, e**), with corresponding increases in MHW frequency (**Fig. S5**). At the same time, a growing fraction of total precipitation occurs as rain rather than snow (**Fig. 4a, d**), consistent with observed warming trends over Svalbard[36]. This snow-to-rain transition accelerates surface melt, weakens snowpack insulation, and reduces surface albedo, thereby reinforcing sea ice loss in the Atlantic Arctic sector[37,38].

Over northern Europe, the negative GH phase is associated with reduced cloud cover, which enhances downward shortwave radiation through cloud radiative effects (**Extended Data Fig. 6-7**) and increases the likelihood and intensity of summer heat extremes (**Fig. 4c, f**). In contrast, the PAS exhibits a markedly different response. Although cyclonic activity also increases during the weak GH phase (**Extended Data Fig. 8c**), colder background conditions favour snowfall over rainfall (**Fig. 4a, d**). Enhanced snow accumulation increases surface albedo and promotes sea ice retention through snow-albedo feedback. These contrasting responses to intensified storm activity likely reflect differences in cyclone origin and structure [39]: storms of mid-latitude origin enhance poleward heat and moisture transport, whereas high-latitude-origin cyclones may suppress net heat transport into the Arctic.

Discussion

This study identifies a fundamental shift in the relationship between the Greenland High (GH) and summer Arctic sea ice around 2004. This timing coincides with the emergence of the "New Arctic", a regime characterized by thinner, younger, and more mobile sea ice[2,40] (see also **Extended Data Fig. 3**). The marked strengthening of the June GH–September SIE correlation provides clear evidence for a regime shift in atmosphere–sea ice coupling. During 2004–2012, persistent GH strengthening accelerated summer sea ice loss, whereas its subsequent weakening after 2012 contributed substantially to the observed slowdown. This result reframes the post-2012 slowdown not as a weakening of atmospheric influence, but rather as the outcome of intensified coupling to a circulation pattern that has itself weakened. Notably, this slowdown is spatially asymmetric: it is dominated by sea ice retention over the Pacific Arctic sector, while the Atlantic Arctic sector and adjacent continental regions have experienced amplified warming and more frequent climate extremes, reflecting a pronounced dipole-like response across the Arctic system (**Fig. 5**).

Feedbacks and intra-seasonal persistence

A key question raised by our findings is what sustains the enhanced intra-seasonal persistence of the GH during the "New Arctic" period? Transfer entropy analysis provides preliminary evidence for a feedback pathway: while the dominant information flow runs from the atmosphere to sea ice (GH to SIE), the reverse direction (SIE to GH) also emerges during P2, suggesting that the coupling becomes bidirectional as ice thins (see **Supplementary Information**). This is consistent with a positive sea ice–atmosphere feedback, whereby initial GH-driven sea ice loss expands spatially through summer (**Fig. 2f-g**), and the resulting increase in open water and reduction in surface albedo feed back onto the atmosphere to reinforce and prolong the GH anomaly. This interpretation is supported in atmospheric model experiments demonstrating that prescribed summer Arctic sea ice loss can induce an elevated GH[41]. Such feedback between GH-driven sea ice loss and the maintenance of the GH anomaly provides a plausible explanation for the observed increase in atmospheric persistence during 2004–2025, and the emergence of a detectable reverse information flow in P2 suggests this feedback has become an active component of the coupled system. The detailed processes governing this feedback on intra-seasonal timescales remain insufficiently understood and warrant targeted investigation using controlled sea ice–forcing experiments.

Connections to large-scale climate variability

On decadal timescales, the recent weakening of the GH and the concurrent shift toward a more positive NAO phase appear linked to multidecadal variability within the Atlantic basin. Wang et al. showed that September Arctic sea ice variability is tightly coupled with summer NAO on interdecadal timescales ($r = 0.92$), with the Atlantic Multidecadal Oscillation (AMO) exerting a dominant influence through modulation of storm tracks and wave–mean flow interactions[24]. During the positive AMO phase, enhanced meridional sea surface temperature gradients increase atmospheric baroclinicity and transient eddy activity, favoring NAO-like circulation anomalies[42,43]. The AMO transitioned into a warm phase during the 1990s and has shown signs of weakening since the early 2010s, potentially contributing to the observed GH weakening.

In parallel, tropical Pacific variability provides an additional pathway influencing Arctic circulation. Yu et al. demonstrated that accelerated North Pacific warming can excite a Rossby wavetrain propagating into the Arctic, driving a downward trend in the summer Arctic Dipole and favoring sea ice retention[23]. The Pacific Decadal Oscillation (PDO) and Interdecadal Pacific Oscillation (IPO) modulate these tropical–extratropical teleconnections[44,45]. The evolving phase and interaction of these basin-scale modes likely acted in concert to favor weaker GH conditions after 2012. Importantly, our results indicate that because atmosphere–sea ice coupling has intensified, future phase shifts in these modes will exert amplified impacts on Arctic sea ice variability.

Implications for prediction and projection

The Arctic has entered a regime in which enhanced atmosphere–sea ice coupling fundamentally alters system behavior. The contemporary sea ice cover increasingly resembles an expansive marginal ice zone[46], rendering it more vulnerable to mechanical disruption by

atmospheric forcing and ocean waves, which fracture ice, mobilize floes, and accelerate lateral melt[47]. This regime shift presents both opportunities and risks for prediction. On the one hand, strengthened coupling may enhance seasonal forecast skill if adequately represented, as early-summer atmospheric conditions become more strongly linked to end-of-summer sea ice outcomes[10,48]. On the other hand, diminished sea ice resilience implies that more persistent circulation anomalies can drive disproportionately large ice losses and potentially trigger cascading climate extremes[49].

Current climate models exhibit substantial spread in their representation of high-latitude atmospheric variability, particularly for the GH and NAO[50-52], and many models underestimate the magnitude and persistence of Greenland blocking events[53]. Our analysis of the CESM2 Large Ensemble corroborates this concern: the model produces near-zero GH–SIE correlations, with the observed P2 coupling ($r = -0.80$) falling outside the entire 100-member ensemble range (**Fig. S6**), suggesting that the model systematically underestimates atmosphere–sea ice coupling sensitivity. This discrepancy likely reflects compounding biases in simulated ice thickness, atmospheric blocking frequency, and ice-albedo feedbacks. Our findings highlight that climate models need to capture not only the mean behavior of Arctic circulation, but also its evolving coupling with sea ice. Failure to represent the processes that intensify this coupling will lead to systematic underestimation of the Arctic's growing susceptibility to circulation-driven extremes. Targeted evaluation of atmosphere–sea ice coupling processes in CMIP6 and the forthcoming CMIP7 framework is therefore a critical priority for improving projections of Arctic change and its global consequences.

Data and Methods

Datasets

Sea ice concentration (SIC). Monthly SIC data for 1979–2025 are obtained from the NSIDC Climate Data Record (CDR) version 4, which combines estimates from the NASA Team and Bootstrap algorithms applied to passive microwave brightness temperatures from SMMR, SSM/I, and SSMIS sensors[54]. The data are provided on a 25 km polar stereographic grid.

Sea ice extent (SIE). SIE is defined as the total area of grid cells with at least 15% SIC.

Sea ice thickness (SIT) and sea ice drift (SID). Monthly SIT and SID data for 1979–2025 are obtained from the Pan-Arctic Ice Ocean Modeling and Assimilation System (PIOMAS)[55], which is a coupled ice–ocean model assimilation system forced by NCEP–NCAR reanalysis. PIOMAS SIT compares well with submarine observation and satellite retrieval[56].

Sea ice age (SIA). Weekly SIA data (1984–2024) at 12.5 km resolution are obtained from NSIDC[57] and converted to a monthly time series.

ERA5 reanalysis. Monthly and daily ERA5 reanalysis data (1979–2025)[58] include mean sea level pressure (SLP), winds, specific humidity, temperature, geopotential height at 500 hPa (Z500), total column water vapor, rainfall and snowfall, and surface radiative fluxes, are obtained from ECMWF.

CERES. Monthly surface radiative fluxes and cloud cover from the Clouds and the Earth's Radiant Energy System (CERES) for March 2000–September 2025[59] are extracted from the level-2B FLXHR product at 1° × 1° resolution.

CESM2-LE. We use simulations from the Community Earth System Model, version 2, Large Ensemble (CESM2-LE)[60,61]. CESM2-LE has a nominal horizontal resolution of 1° and comprises 100 ensemble members initialized from different combinations of atmosphere and ocean states. The simulations are forced by CMIP6 historical forcing from 1850 to 2014 and the Shared Socioeconomic Pathway SSP3-7.0 scenario from 2015 to 2100. For comparison with observations, we analyze the periods P1 (1980–2003) and P2 (2004–2025), extracting June Greenland High indices and September sea ice extent from each ensemble member.

Climate indices

Greenland High (GH). The GH index is defined as the area-weighted average of geopotential height at 500 hPa over Greenland (60°–80°N, 20°–80°W) following Hanna et al.[15].

Arctic Dipole (AD). The AD is defined as the second EOF mode of SLP anomalies (relative to 1991–2020 climatology) north of 70°N based on ERA5 (1979–2025), following Wu et al.[62].

North Atlantic Oscillation (NAO) and Arctic Oscillation (AO). The NAO is defined as the leading EOF of SLP anomalies over the Atlantic sector (20°–80°N, 90°W–40°E); the AO is defined as the leading EOF of SLP anomalies north of 20°N. Both indices are obtained from the NOAA Climate Prediction Center.

Derived metrics

Marine heatwaves (MHW). MHW are identified following Hobday et al.[63], using a seasonally varying 90th percentile threshold and requiring persistence of at least five consecutive days. MHW intensity is defined as the mean temperature anomaly above the threshold during MHW events; frequency is the number of MHW events per season.

Atmospheric heat extremes. Hot extremes over land are identified using ERA5-Land 2-m temperature data[64]. For each grid cell and calendar day, a hot threshold (C90) is established at the 90th percentile of the temperature distribution from a 31-day window throughout the reference period (1981–2010). Daily hot extreme intensity is quantified as the temperature surplus above C90, subject to a temporal filter requiring at least three consecutive days.

Rainfall ratio. The rainfall ratio is defined as (total precipitation − snowfall) / total precipitation based on ERA5.

Eddy kinetic energy (EKE). EKE quantifies synoptic-scale atmospheric variability at 850 hPa, calculated as

$$EKE = (\sqrt{u'^2 + v'^2}),$$

where u' and v' are high-pass filtered (2–8 day) zonal and meridional wind anomalies.

Top-of-Atmosphere Cloud Radiative Effect (TOA CRE). The TOA CRE quantifies the influence of clouds on Earth's radiation budget, calculated as

$$CRE = R_{clear} - R_{all-sky},$$

where R_{clear} is the clear-sky radiative flux, and $R_{all-sky}$ is the all-sky radiative flux at the top of the atmosphere. The net CRE is decomposed into shortwave (SW) and longwave (LW) components:

$$CRE_{net} = CRE_{sw} + CRE_{lw},$$

where CRE_{sw} (typically negative) represents the cooling effect from cloud reflection of incoming solar radiation, and CRE_{lw} (typically positive) represents the warming effect from cloud absorption and re-emission of outgoing longwave radiation.

Surface energy balance. The net surface heat flux (Net SHF) is calculated as the sum of net longwave radiation flux ($netLW$), net shortwave radiation flux ($netSW$), latent heat flux (LHF), and sensible heat flux (SHF):

$$\text{Net SHF} = netLW + netSW + LHF + SHF.$$

By convention, negative values imply a heat loss of the surface and positive values imply a heat gain for each term in the formula. We utilize ERA5 data to derive these flux components for analyzing temporal patterns in the surface heat flux.

Change point detection. To objectively identify regime shifts in the Greenland High–sea ice extent correlation time series, we employ two complementary approaches. First, we apply the Pruned Exact Linear Time (PELT) algorithm with the Bayesian Information Criterion (BIC) penalty. This approach detects change points in the mean by minimizing BIC, which balances model fit against complexity to determine the optimal number of breakpoints without over-fitting. Second, we use segmented regression analysis, which identifies breakpoints by minimizing the total residual sum of squares across piecewise linear segments. This method detects structural changes in the linear relationship over time, complementing the mean-shift detection of the PELT algorithm. Both algorithms are applied to the 11-year running correlation between detrended June GH index and detrended September SIE over 1979–2025. Statistical significance of differences between identified periods is assessed using Welch's t-test for means (accounting for unequal variances) and F-test for variances. Periods with statistically distinguishable means ($p < 0.05$) are considered distinct regimes.

GH contribution estimation. The contribution of GH variability to the post-2012 slowdown is estimated using linear regression over P2 (2004–2025). Both the September SIE and the June GH index are linearly detrended over the full record (1979–2025) before performing the regression. Detrending is essential to isolate the interannual covariance between GH and SIE from spurious correlations that can arise when two time series share similar long-term trends driven by external forcing (e.g., anthropogenic warming); without detrending, the forced component of sea ice decline could be erroneously attributed to atmospheric circulation variability. The GH-attributed SIE anomaly is calculated as the product of the regression

coefficient and the detrended GH index change between the strong GH phase (2007–2012) and the weak GH phase (2013–2025). This attributed anomaly is then expressed as a percentage of the detrended SIE difference between periods, yielding the ~70% contribution estimate. Sensitivity analyses using different detrending approaches (quadratic, piecewise linear) and period definitions (i.e., 2004–2012) yielded consistent results (57–70%).

Data Availability

Sea ice concentration, sea ice extent, and sea ice age are available from the National Snow and Ice Data Center (https://nsidc.org). PIOMAS sea ice thickness and motion data are available from the Polar Science Center (http://psc.apl.uw.edu/research/projects/arctic-sea-ice-volume-anomaly/). ERA5 is retrieved from the Copernicus Climate Data Store (https://cds.climate.copernicus.eu). CERES data are available from NASA (https://ceres.larc.nasa.gov). The NAO and AO indices are available from NOAA PSL (https://psl.noaa.gov/gcos_wgsp/Timeseries/). The ERA5-Land-based hot extremes are available from the website (https://doi.org/10.11888/Atmos.tpdc.302636). The CESM2-LE model output is available through https://www.cesm.ucar.edu/projects/community-projects/LENS2/data-sets.html.

Code Availability

Code used for data analysis and figure generation is fully based on Python and is available upon reasonable request from the corresponding authors.

Author Contributions

All authors contributed to the conception and design of the study, data analysis, interpretation of results, and writing of the manuscript.

Competing Interests

The authors declare no competing interests.

Acknowledgments

This research was supported by the National Key R&D Program of China (2021YFC2802504) and Tsinghua University (100008001). Shengping He acknowledges the BASIC project (grant No. 325440) funded by the Research Council of Norway and the Nansen Center's basic institutional funding through the Research Council of Norway (grant No. 342624).

Figures

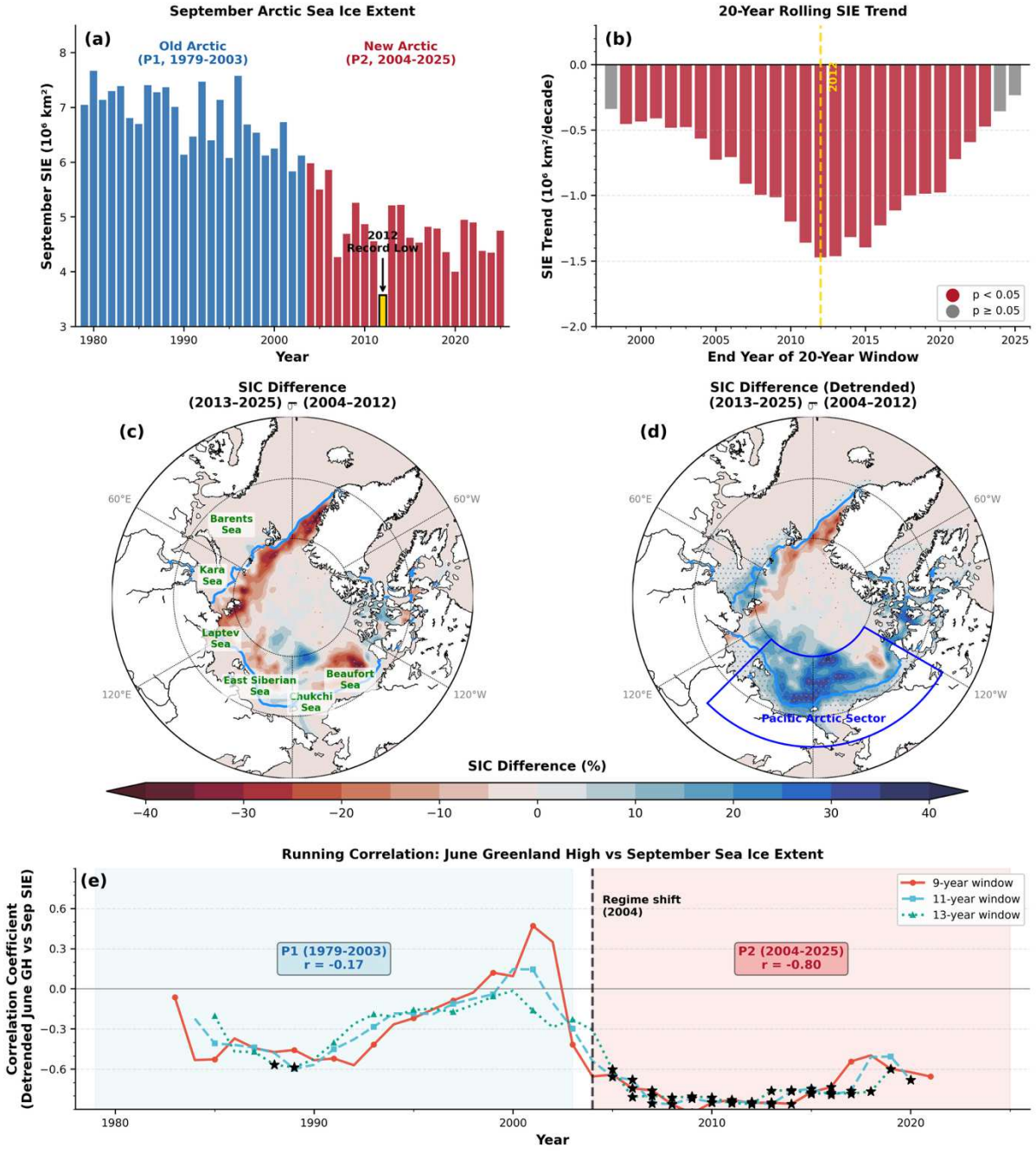


Figure 1 | Post-2012 slowdown in September Arctic sea ice decline and strengthening atmosphere–sea ice coupling. (a) Time series of September Arctic sea ice extent (SIE) for 1979–2025. Bars are coloured by regime: Period 1 (P1; 1979–2003, blue) and Period 2 (P2; 2004–2025, red). The 2012 record low is marked with a star. **(b)** Evolution of 20-year rolling SIE trends as a function of the end year of each window. Filled red bars indicate statistically significant trends ($p < 0.05$); grey bars indicate non-significant trends. **(c)** Difference in September sea ice concentration (SIC) between the weak Greenland High (GH) phase (2013–2025) and the strong GH phase (2004–2012). **(d)** As in **(c)**, but for detrended SIC to isolate interannual variability from the long-term trend. In **(c)** and **(d)**, stippling denotes statistically significant differences ($p < 0.05$, two-sided t-test), and the blue contour marks the

climatological sea ice edge (15% SIC, 1991–2020). **(e)** Running correlations between detrended June GH and detrended September Arctic sea ice extent (SIE), calculated using 9-year (orange), 11-year (blue), and 13-year (green) sliding windows. Black stars denote correlations significant at $p < 0.05$. The vertical dashed line marks the regime shift identified by change point detection (~2004). Background shading indicates P1 (light blue) and P2 (light red); inset boxes show period-mean correlations (P1: $r = -0.17$; P2: $r = -0.80$), **highlighting the pronounced strengthening of the GH–SIE relationship following the regime transition.**

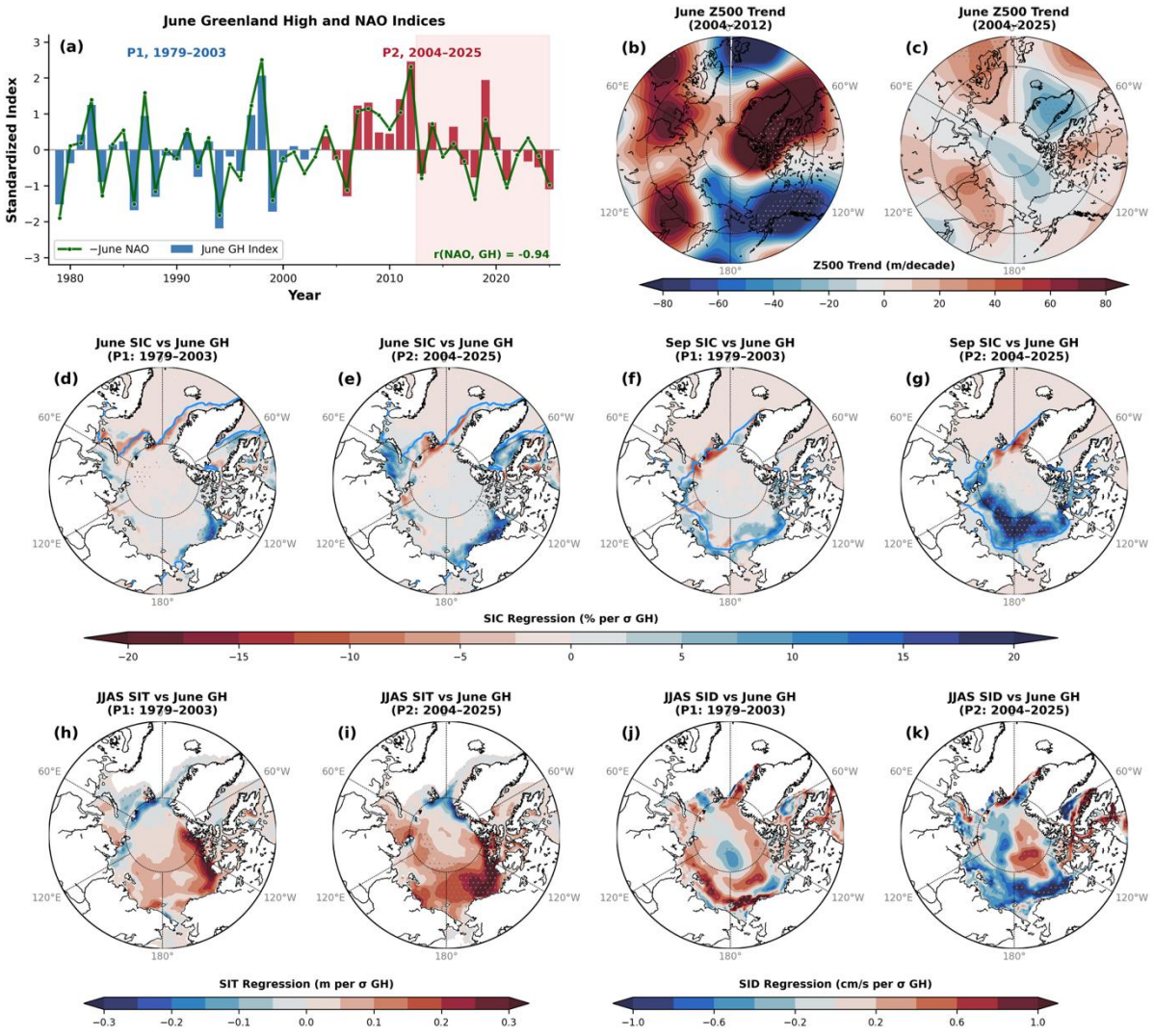


Figure 2 | Evolution of the Greenland High and its strengthening influence on Arctic sea ice. (a) Standardized June Greenland High (GH) and inverted North Atlantic Oscillation (−NAO) indices for 1979–2025. Bars are coloured by regime: P1 (1979–2003; blue) and P2 (2004–2025; red). Light red shading denotes the post-2012 period characterized by persistent GH weakening. **(b)** Linear trend in June 500-hPa geopotential height (Z500) during 2004–2012, corresponding to anomalously strong GH conditions. **(c)** As in **(b)**, but for 2004–2025, illustrating the trend reversal associated with GH weakening after 2012. Stippling in **(b)** and **(c)** indicates statistically significant trends ($p < 0.05$). **(d–g)** Regression of sea ice concentration

(SIC) onto the sign-reversed standardized June GH index (–GH) for June **(d, e)** and September **(f, g)** during P1 **(d, f)** and P2 **(e, g)**. Positive (blue) and negative (red) values indicate increased and decreased SIC associated with a stronger GH, respectively. Stippling marks grid cells with statistically significant regressions ($p < 0.05$, two-tailed t-test). The solid blue contour denotes the climatological sea ice edge (15% SIC threshold; 1991–2020 mean). During P2, the GH–SIC relationship intensifies and expands spatially, particularly across the Pacific Arctic marginal seas (Chukchi, Beaufort, and East Siberian Seas). **(h, i)** As in **(d–g)**, but for summer-mean (JJAS) sea ice thickness (SIT). **(j, k)** As in **(d–g)**, but for summer-mean (JJAS) sea ice drift speed. All regressions are expressed per standard deviation of –GH and both time series are linearly detrended prior to analysis. **During P2, the GH–sea ice coupling intensifies and expands spatially, particularly across the Pacific Arctic marginal seas (Chukchi, Beaufort, and East Siberian Seas), demonstrating that Arctic sea ice has become increasingly responsive to Greenland High variability as the ice cover has transitioned to a thinner, younger state.**

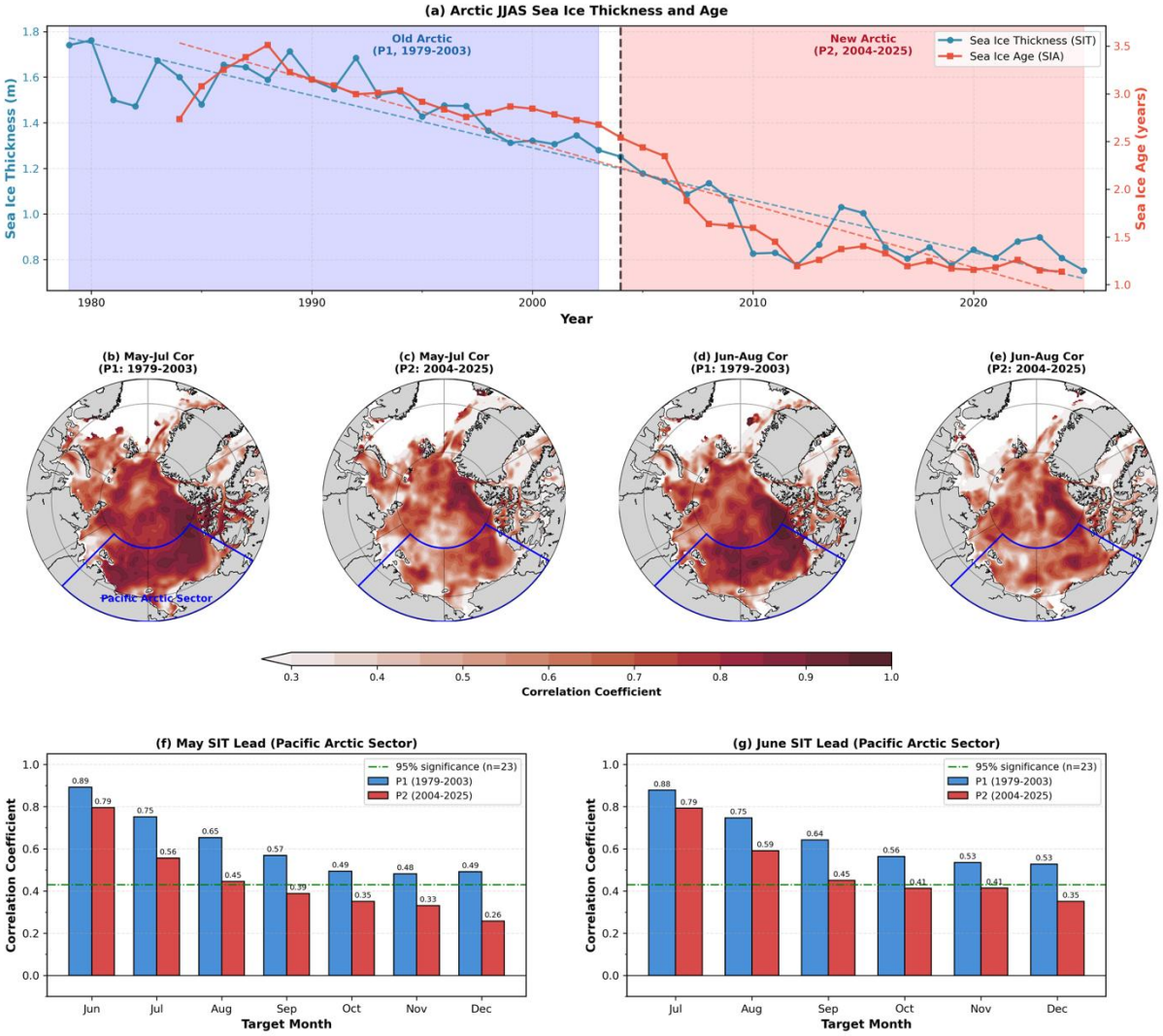


Figure 3 | Transition to thinner, younger Arctic sea ice and reduced intra-seasonal persistence. (a) Time series of summer-mean (JJAS) Arctic sea ice thickness (SIT; blue, left axis) from PIOMAS and sea ice age (SIA; red, right axis) from NSIDC. Dashed lines denote linear trends. Light shading distinguishes Period 1 (P1; 1979–2003, blue) from Period 2 (P2; 2004–2025, red). **(b–e)** Spatial correlation coefficients of monthly SIT between **(b)** May and July during P1, **(c)** May and July during P2, **(d)** June and August during P1, and **(e)** June and August during P2. The blue box outlines the Pacific Arctic sector (65–80°N, 135–240°E). **(f, g)** Lagged correlations of SIT averaged over the Pacific Arctic sector, with May **(f)** and June **(g)** as lead months and subsequent months through December as lagged targets. Blue and red bars represent P1 and P2, respectively. The green dashed line indicates the 95% significance threshold (r = 0.42 for n = 22). **The widespread reduction in correlation coefficients from P1 to P2 reflects a substantial decline in sea ice thickness persistence, consistent with the emergence of a younger, more mobile ice cover that responds more rapidly to atmospheric forcing.**

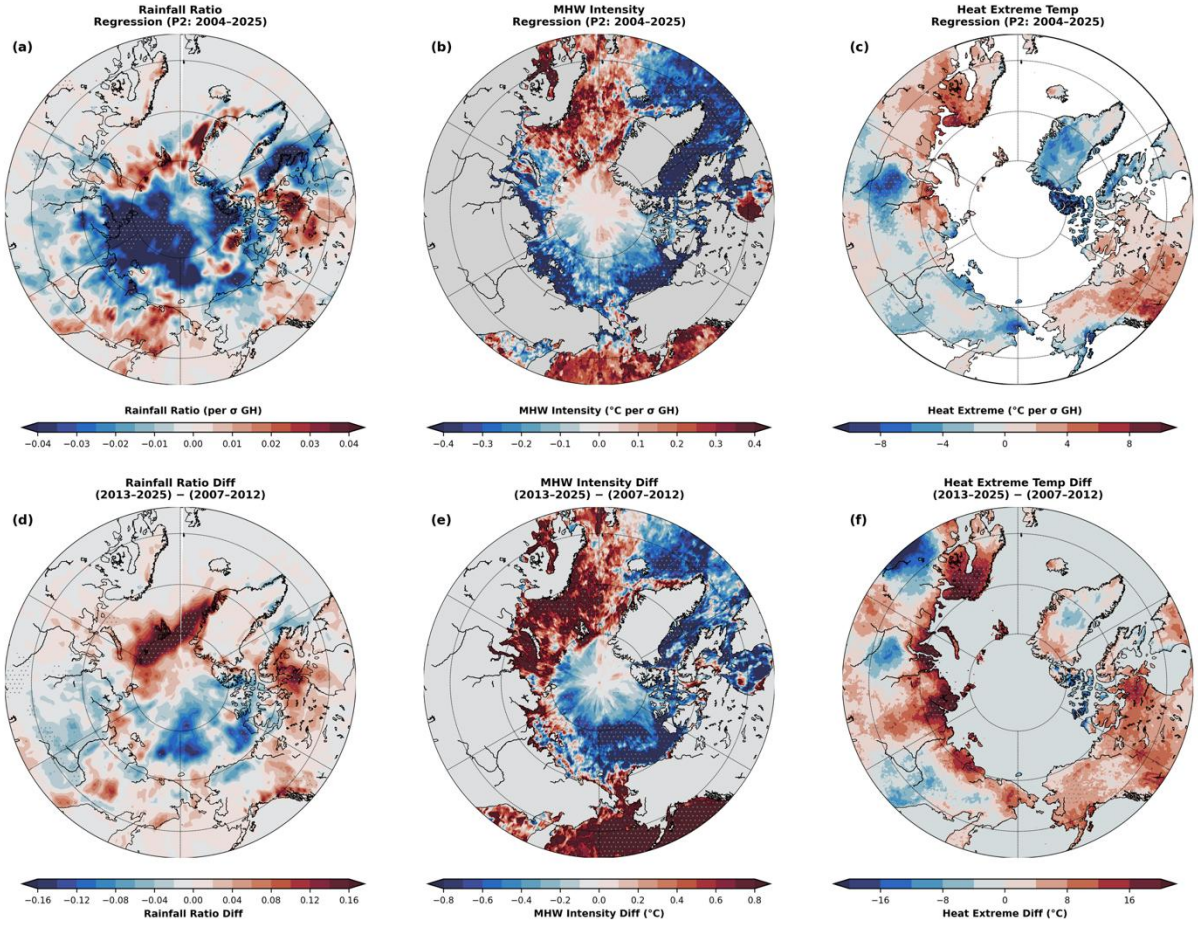


Figure 4 | Downstream climate impacts of Greenland High variability and weakening. (a–c) Regression of summer-mean (JJAS) climate variables onto the detrended, sign-reversed June Greenland High (GH) index during 2004–2025: **(a)** rainfall ratio (fraction of total precipitation falling as rain), **(b)** mean marine heatwave (MHW) intensity, and **(c)** accumulated temperature of compound hot extremes. Negative regression coefficients (blue) indicate that weaker GH conditions are associated with increases in these variables. **(d–f)** Composite differences between the weak GH phase (2013–2025) and the strong GH phase (2007–2012) for **(d)** rainfall ratio (shading), overlaid with total precipitation differences (blue contours; solid lines indicate increases and dashed lines indicate decreases), **(e)** MHW intensity, and **(f)** compound hot-extreme accumulated temperature. Stippling denotes statistically significant differences ($p < 0.05$; two-tailed t-test for regressions in **a–c** and independent two-sample t-test for composites in **d–f**). All regressions are expressed per standard deviation of the −GH and both time series are linearly detrended. **These patterns demonstrate that post-2012 GH weakening is linked to an increased rainfall fraction over the East Greenland Sea and northern Barents Sea, intensified marine heatwaves in the Norwegian–Barents Seas, and amplified summer heat extremes across northern Europe and northwestern Siberia.**

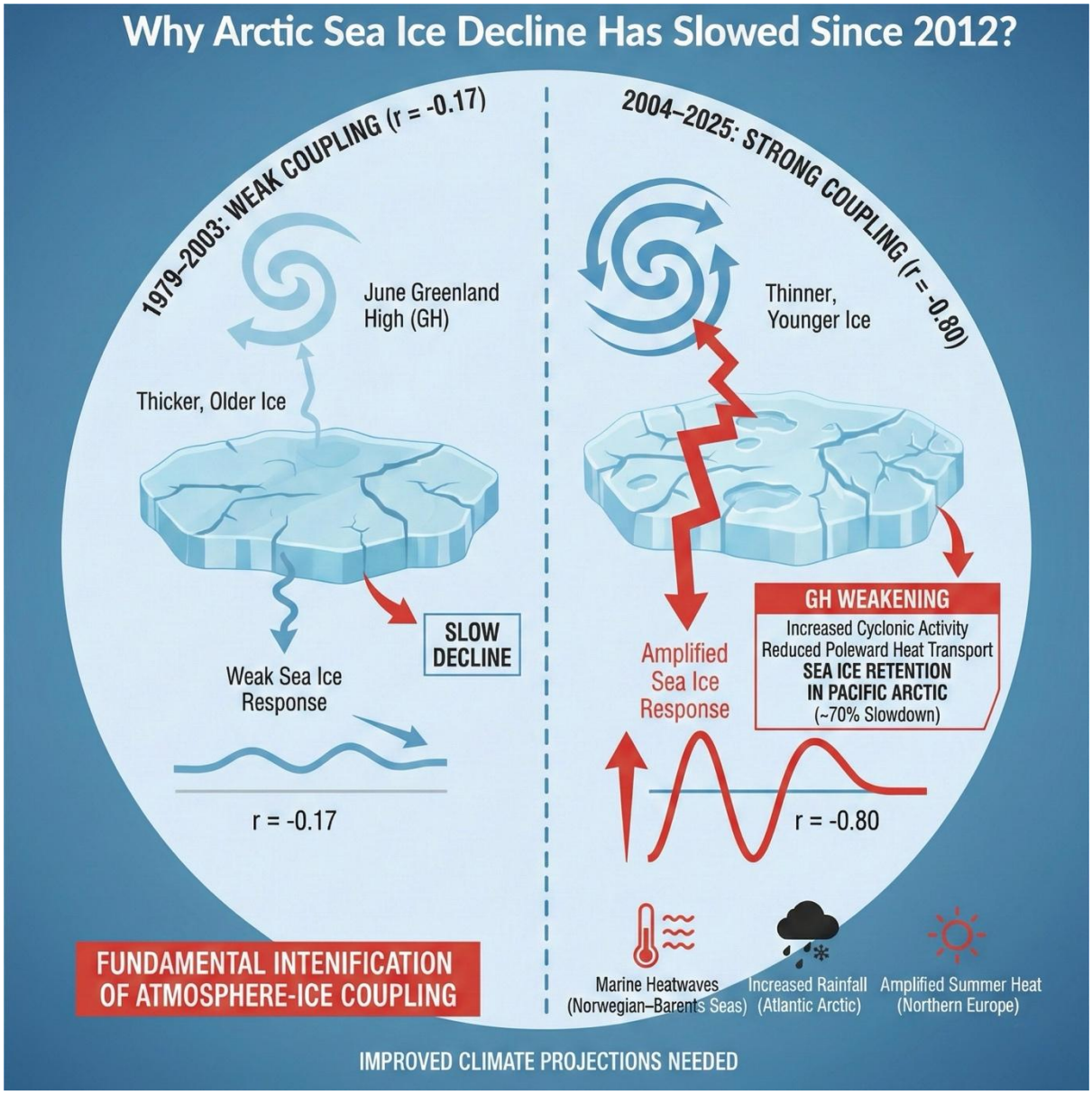
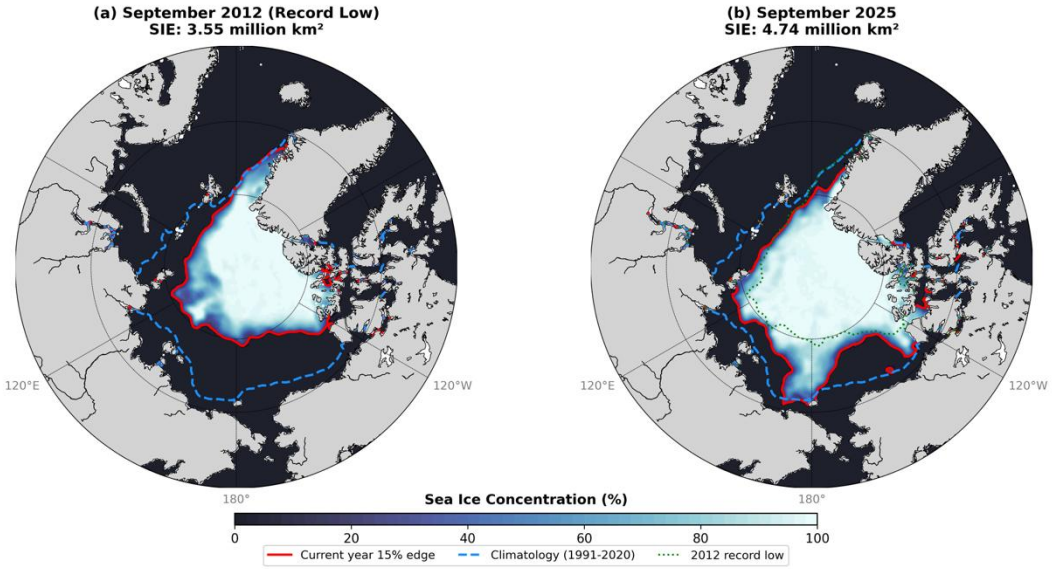
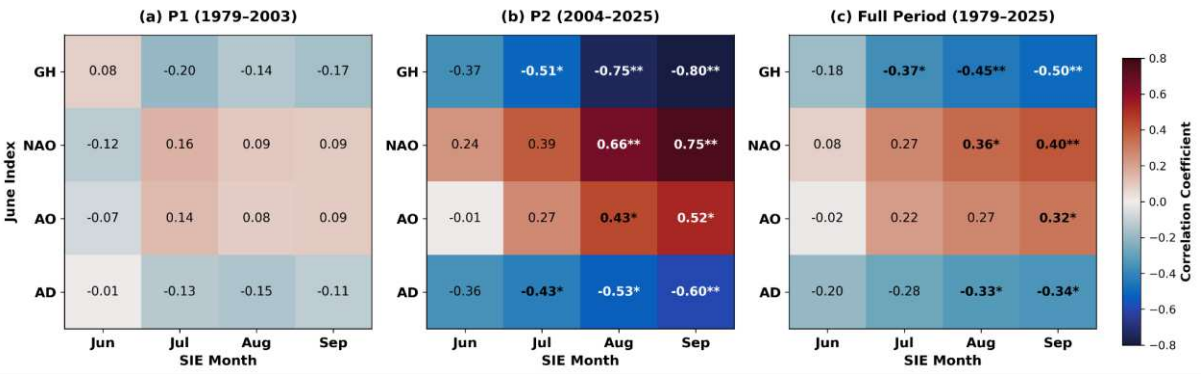


Figure 5 | Schematic of the regime shift in Greenland High–sea ice coupling and its implications for the post-2012 slowdown and downstream climate extremes. During the strong-GH phase (2007–2012), persistent positive GH anomalies promote anticyclonic circulation over the Arctic, enhancing poleward heat and moisture transport, reducing cloud cover, and increasing surface shortwave absorption, all of which accelerate summer ice melt. During the weak-GH phase (2013–2025), negative GH anomalies favor cyclonic activity and increased snowfall over the Canadian Arctic Basin while reducing poleward heat transport, thereby promoting sea ice retention in the Pacific Arctic sector. The intensified GH–SIE coupling in P2 ($r = -0.80$ vs. $r = -0.17$ in P1) means that GH variability now exerts amplified influence on both Arctic sea ice and downstream climate. Weak GH conditions simultaneously favor Arctic sea ice retention and intensified midlatitude extremes, including marine heatwaves in the Norwegian–Barents Seas, enhanced rainfall over the Atlantic Arctic, and summer heat extremes over Northern Europe.

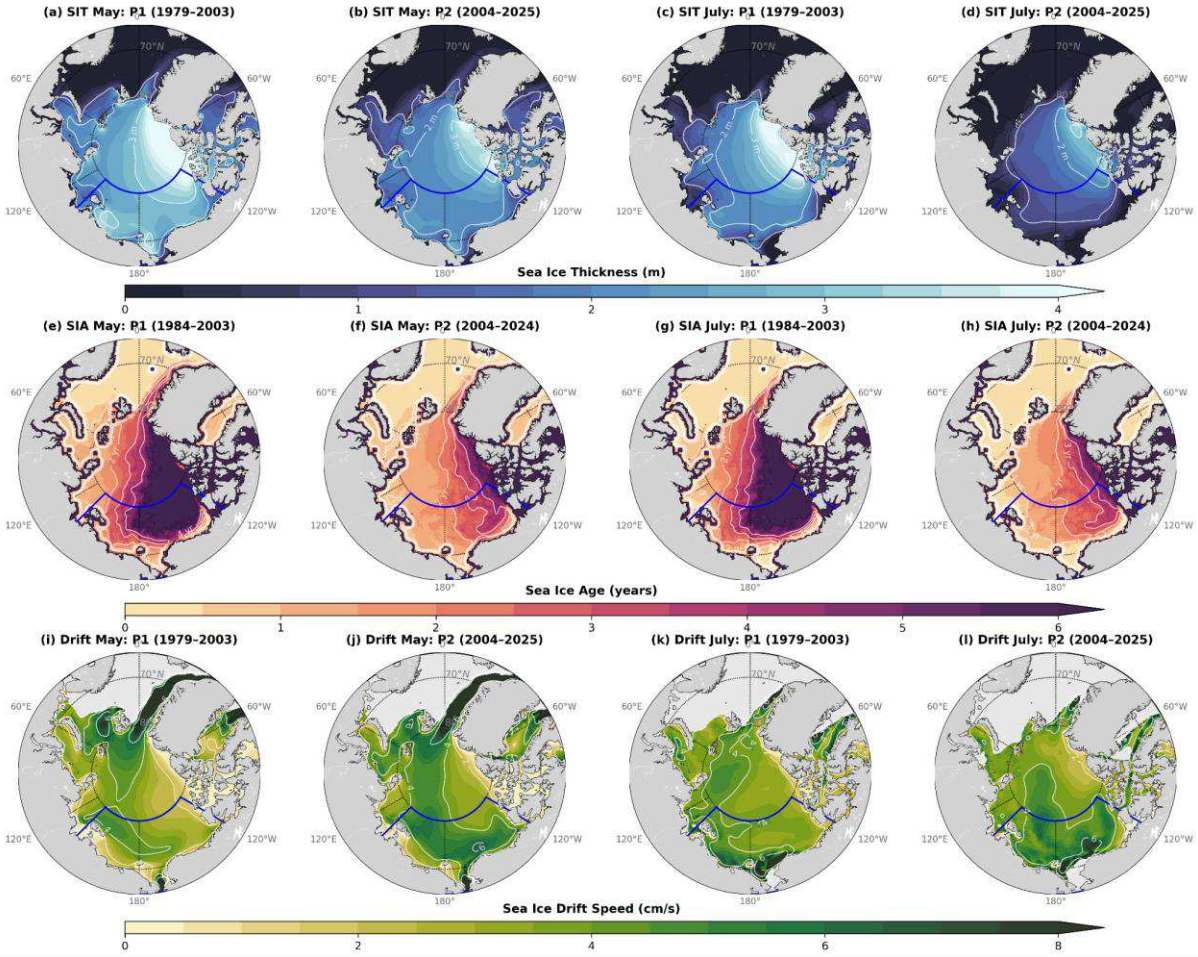
Extended Data Figures



Extended Data Figure 1 | Comparison of September Arctic sea ice concentration between the 2012 record low and 2025. (a) September 2012, which holds the satellite-era record for lowest sea ice extent. **(b)** September 2025. Shading shows sea ice concentration (%). The red solid line indicates the 15% sea ice concentration edge for each respective year. The blue dashed line shows the 1991–2020 climatological sea ice edge. In panel **(b)**, the green dotted line shows the 2012 record low edge for reference. Sea ice extent values are calculated as the total area of grid cells with concentration ≥15%. Despite the post-2012 slowdown in the rate of sea ice decline, September 2025 SIC remains at low levels across the Pacific Arctic Sector, indicating that the observed deceleration represents a reduced rate of sea ice loss rather than recovery of sea ice extent.



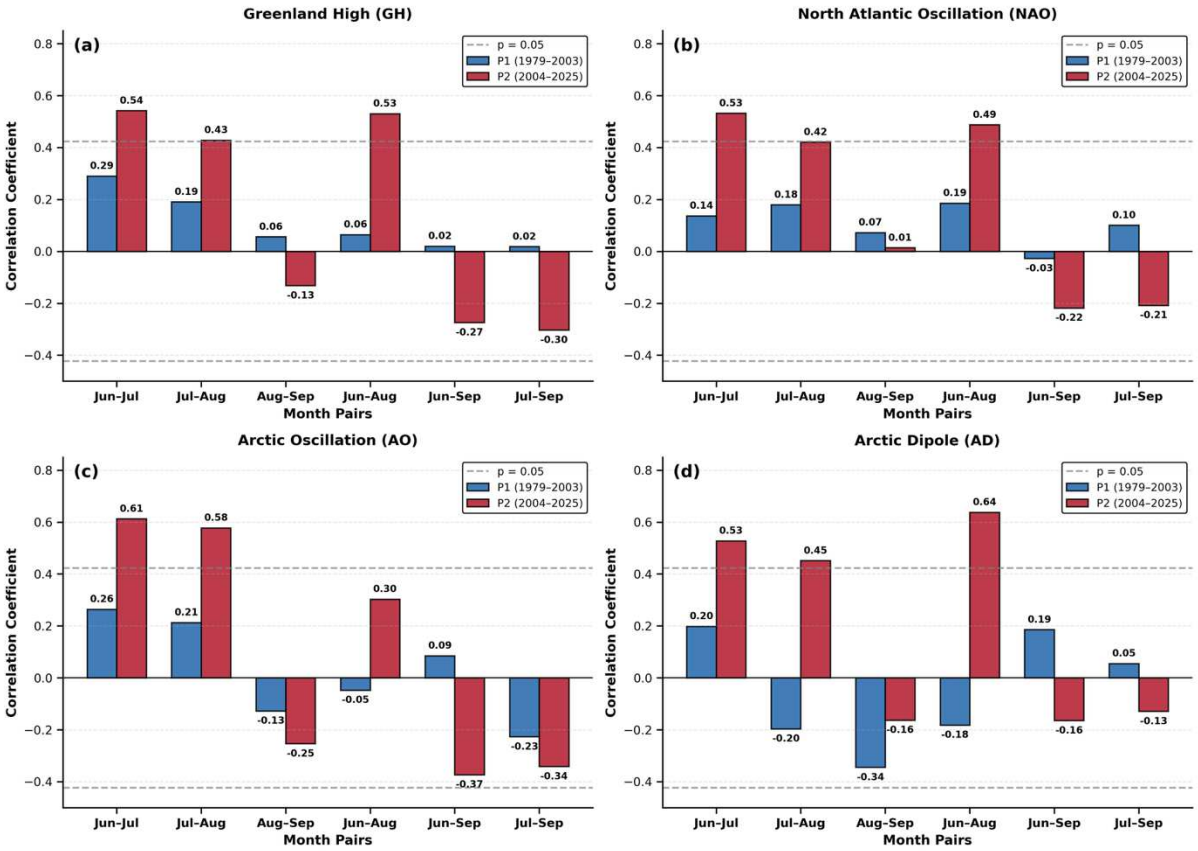
Extended Data Figure 2 | Correlation between June atmospheric circulation indices and Arctic sea ice extent (SIE). Heatmaps showing Pearson correlation coefficients between June values of the Greenland High (GH), North Atlantic Oscillation (NAO), Arctic Oscillation (AO), and Arctic Dipole (AD) indices and monthly Arctic SIE from June through September for **(a)** P1 (1979–2003, n=25), **(b)** P2 (2004–2025, n=22), and **(c)** the full period (1979–2025, n=47). All time series are linearly detrended before correlation analysis. Single asterisk (*) denotes significance at $p < 0.05$; double asterisk (**) denotes significance at $p < 0.01$. The GH index shows markedly strengthened negative correlations with ASIE across all summer months in P2 compared to P1, indicating that June GH anomalies have become increasingly predictive of subsequent summer sea ice conditions.



615

616 **Extended Data Figure 3 | Spatial distribution of Arctic sea ice thickness, age, and sea ice**
617 **drift speed. (a–d)** Mean sea ice thickness (SIT, meters) from PIOMAS for May and July during
618 P1 (1979–2003) and P2 (2004–2025). **(e–h)** Mean sea ice age (SIA, years) from NSIDC for
619 May and July during P1 (1984–2003) and P2 (2004–2024). **(i–l)** Mean sea ice drift speed (cm/s)
620 from PIOMAS for May and July during P1 (1979–2003) and P2 (2004–2025). White contours
621 indicate thickness (1, 2, 3 m), age (1, 2, 3, 4 yr), and drift speed (2, 4, 6 cm/s) isolines. Blue
622 boxes denote the Pacific Arctic Sector (65–80°N, 135–240°E). The transition from P1 to P2
623 shows widespread thinning, rejuvenation, and acceleration of Arctic sea ice, with particularly
624 pronounced changes in the Pacific Arctic Sector, where multi-year ice has been largely
625 replaced by thinner, younger, and more mobile first-year ice. The increased drift speed in P2
626 reflects reduced internal ice stress associated with a thinner, less compact ice cover, enhancing
627 the ice pack's responsiveness to wind forcing. These structural changes collectively contribute
628 to the intensified sensitivity of summer sea ice extent to atmospheric circulation variability
629 observed in P2.

630



631

632 **Extended Data Figure 4 | Intra-seasonal persistence of Arctic atmospheric circulation**
633 **indices.** Bar plots showing lag correlations between summer months (June–September) for **(a)**
634 Greenland High (GH), **(b)** North Atlantic Oscillation (NAO), **(c)** Arctic Oscillation (AO), and
635 **(d)** Arctic Dipole (AD). Blue bars: P1 (1979–2003); red bars: P2 (2004–2025). Gray dashed
636 lines indicate the 95% significance threshold (r = 0.42, n = 22). The GH exhibits markedly
637 enhanced persistence in P2 relative to P1, with significant correlations extending from June
638 through September. This strengthened intra-seasonal memory is not unique to the GH; the
639 NAO, AO, and AD all show consistent increases in intra-seasonal persistence.

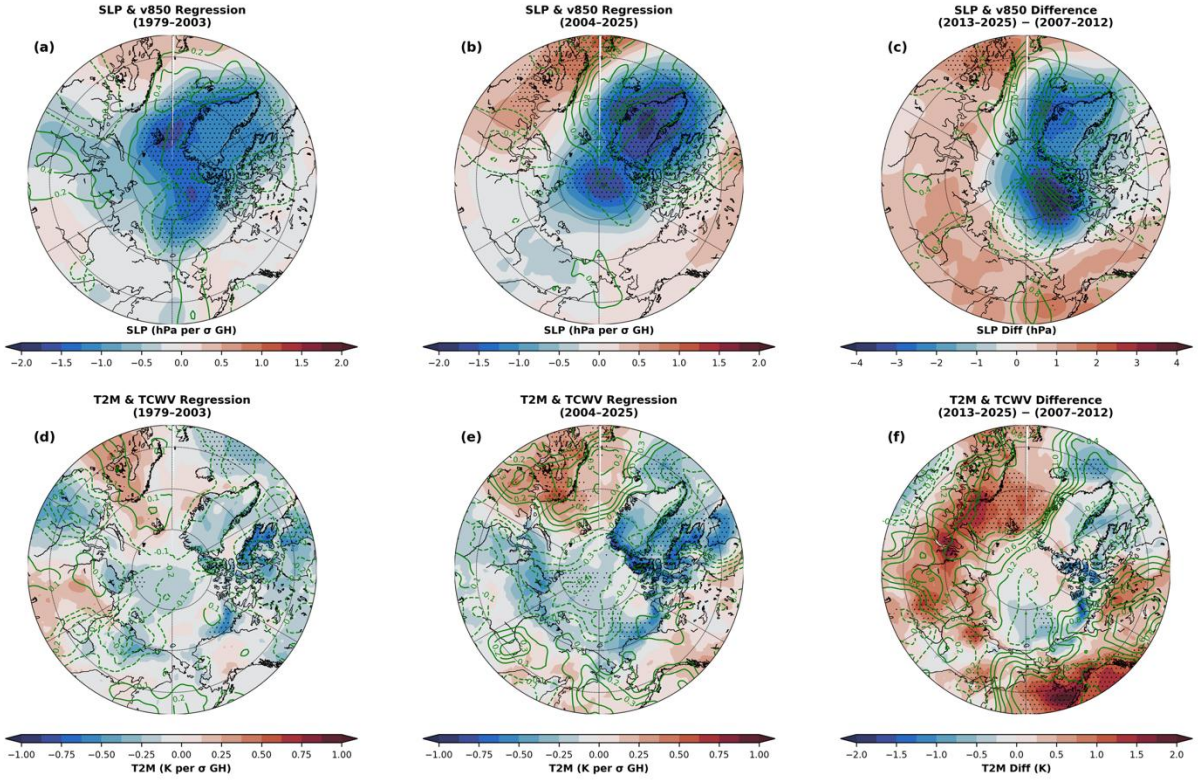
640

641

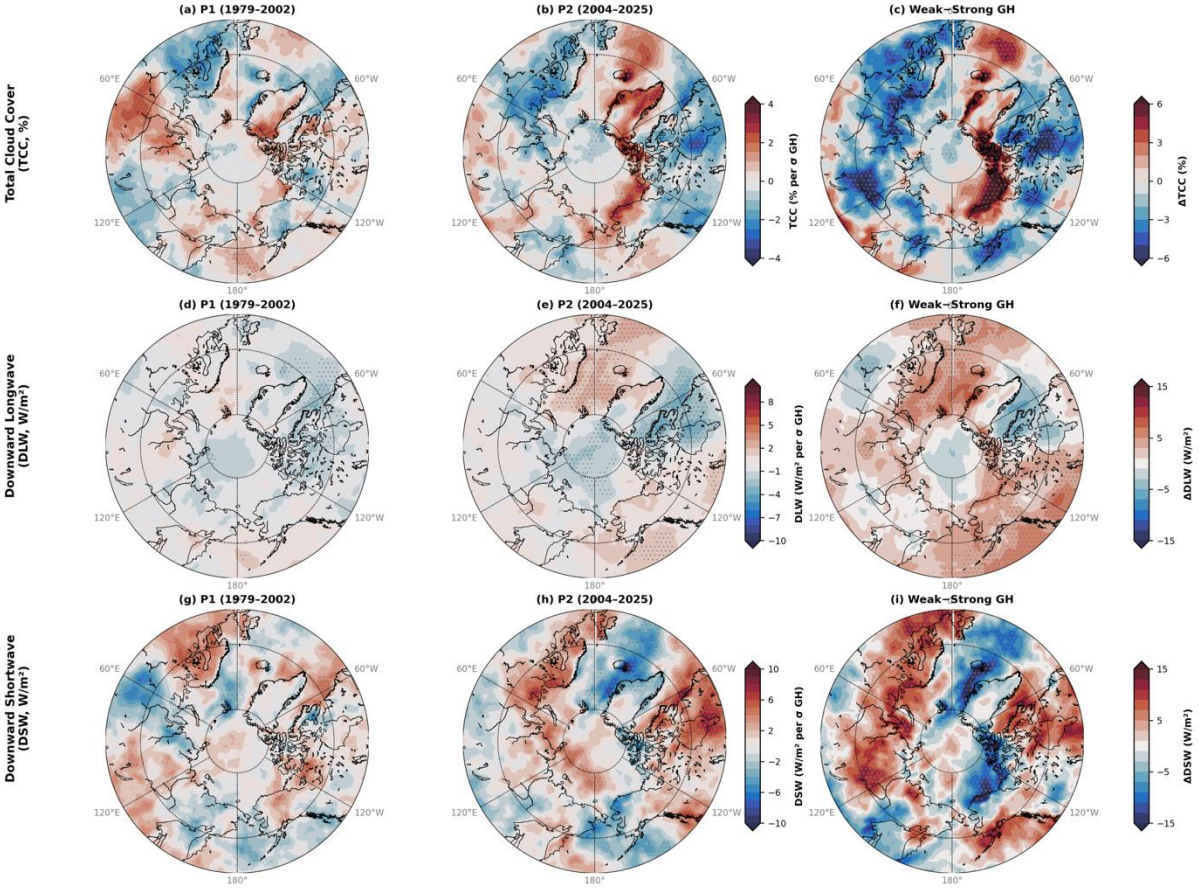
642

643

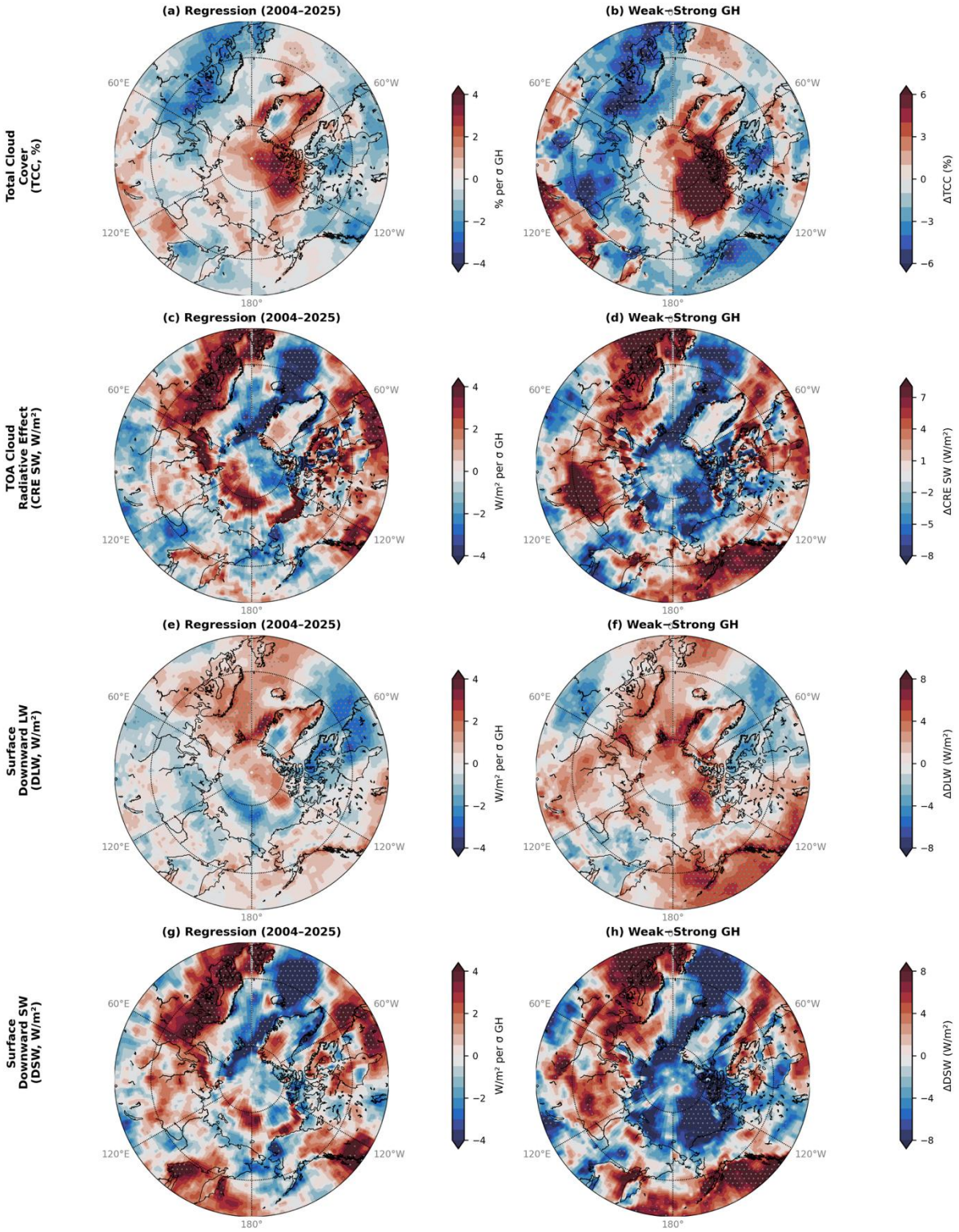
644



Extended Data Figure 5 | Enhanced atmospheric response to Greenland High variability in the recent period. Top row **(a–b)**: Regression of JJAS sea level pressure (SLP, color shading, hPa) and 850-hPa meridional wind (v850, green contours, m/s) onto the detrended June Greenland High (GH) index for **(a)** Period 1 (1979–2003) and **(b)** Period 2 (2004–2025), alongside **(c)** composite mean difference between the weak GH phase (2013–2025) and strong GH phase (2007–2012). Bottom row **(d–e)**: Same as **(a-c)** but for 2-meter temperature (T2M, color shading, K) and total column water vapor (TCWV, green contours, kg/m²). **(c)** and **(f)** show composite differences of the corresponding variables between P2 and P1. Stippling denotes statistical significance at the 95% confidence level ($p < 0.05$; regression t-test for panels **a, b, d, e**; independent two-sample t-test for panels **c, f**). Solid contours indicate positive values; dashed contours indicate negative values. All regressions are expressed per standard deviation of the inverted GH index and both time series are linearly detrended prior to analysis. Comparison between periods reveals substantially strengthened GH–circulation relationships in P2, with enhanced SLP anomalies over the Arctic Ocean and amplified southerly wind anomalies transporting warm, moist air into the Barents–Kara Seas region. The composite differences **(c, f)** confirm that the post-2012 GH weakening is associated with anomalous low pressure over Greenland, increased southerly flow into the Atlantic Arctic, and corresponding surface warming and moistening.



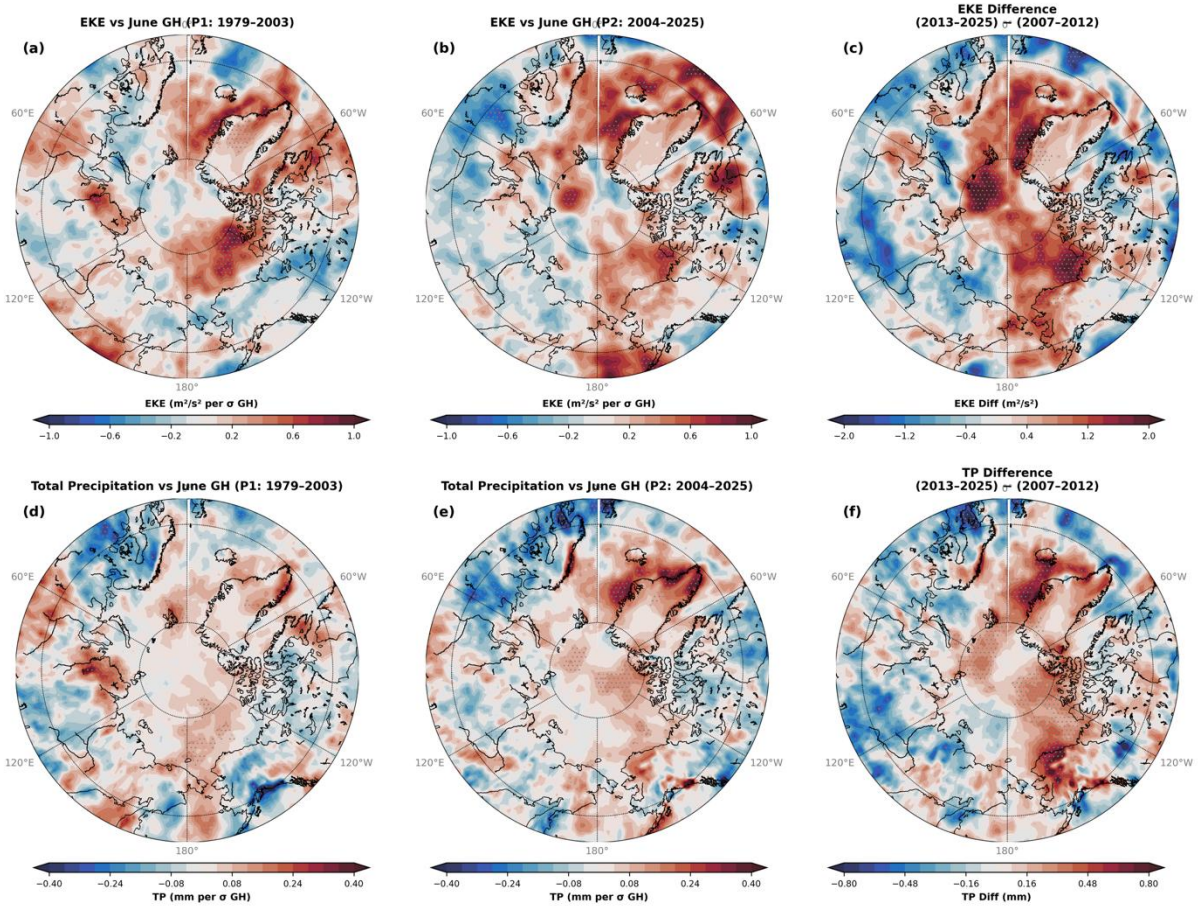
Extended Data Figure 6 | Regression of JJAS cloud cover and surface radiation onto the June Greenland High index. Regression coefficients of total cloud cover (TCC, top row), downward longwave radiation (DLW, middle row), and downward shortwave radiation (DSW, bottom row) onto the detrended June GH index for **(a, d, g)** P1 (1979–2003) and **(b, e, h)** P2 (2004–2025). The right column **(c, f, i)** shows composite mean differences between the weak GH period (2013–2025) and the strong GH period (2007–2012). The GH index is multiplied by −1, so positive regression coefficients indicate anomalies associated with a weakened GH. Stippling denotes statistical significance ($p < 0.05$; regression t-test for columns 1–2; independent two-sample t-test for column 3). All regressions are expressed per standard deviation of the inverted GH index and both time series are linearly detrended prior to analysis. The weakened GH during P2 is associated with increased cloudiness over the central Arctic and Greenland Sea, enhanced downward longwave radiation promoting surface warming, and reduced downward shortwave radiation due to increased cloud cover. These radiative changes contribute to accelerated sea ice loss in the Atlantic Arctic sector while partially offsetting ice melt in the Pacific Arctic sector through reduced solar heating.



682

683 **Extended Data Figure 7 | CERES satellite observations of cloud cover and surface**
684 **radiation response to the June Greenland High variability. (a, c, e, g)** Regression
685 coefficients of JJAS total cloud cover (TCC), TOA cloud radiative effect (CRE SW), surface
686 downward longwave radiation (DLW), and surface downward shortwave radiation (DSW)
687 onto the detrended June GH index for 2004–2025. The GH index is multiplied by −1, so
688 positive values indicate anomalies associated with a weakened GH. **(b, d, f, h)** Composite mean

differences between the weak GH period (2013–2025) and the strong GH period (2007–2012). Stippling denotes statistical significance ($p < 0.05$). Regressions are expressed per standard deviation of the inverted GH index and both time series are linearly detrended prior to analysis. CERES observations confirm that the weakened GH is associated with increased cloudiness, enhanced cloud radiative effects (more negative CRE SW), increased surface longwave warming, and reduced surface shortwave radiation over the Arctic and North Atlantic sectors.



Extended Data Figure 8 | Enhanced storm activity and precipitation response to Greenland High variability. (a–c) Eddy kinetic energy (EKE) at 850 hPa regressed onto the detrended, sign-reversed June Greenland High index (−GH) during **(a)** P1 (1979–2003) and **(b)** P2 (2004–2025), with **(c)** composite difference in summer-mean (JJAS) EKE between the weak-GH phase (2013–2025) and the strong-GH phase (2007–2012). **(d–f)** As in **(a–c)**, but for total precipitation. Positive regression coefficients indicate increased EKE or precipitation associated with GH weakening; negative coefficients indicate decreases. Stippling denotes statistical significance ($p < 0.05$; two-tailed t-test for regressions in **a, b, d, e**; independent two-sample t-test for composites in **c, f**). All regressions are expressed per standard deviation of the inverted GH index and both time series are linearly detrended prior to analysis. During P2, the GH–EKE relationship strengthens over the North Pacific storm-track region, while the GH–precipitation coupling intensifies and expands spatially across the Arctic Ocean and surrounding seas. The transition from strong-GH (2007–2012) to weak-GH (2013–2025) conditions is associated with enhanced storm activity over the Canadian Arctic Basin and East Greenland Sea, accompanied by a coherent increase in precipitation.

References

1 Serreze, M. C. & Meier, W. N. The Arctic's sea ice cover: trends, variability, predictability, and comparisons to the Antarctic. *Annals of the New York Academy of Sciences* **1436**, 36-53 (2019). https://doi.org/https://doi.org/10.1111/nyas.13856

2 Stroeve, J. & Notz, D. Changing state of Arctic sea ice across all seasons. *Environmental Research Letters* **13**, 103001 (2018). https://doi.org/10.1088/1748-9326/aade56

3 Jahn, A., Holland, M. M. & Kay, J. E. Projections of an ice-free Arctic Ocean. *Nature Reviews Earth & Environment* **5**, 164-176 (2024). https://doi.org/10.1038/s43017-023-00515-9

4 Notz, D. & Community, S. Arctic Sea Ice in CMIP6. *Geophys Res Lett* **47** (2020). https://doi.org/10.1029/2019gl086749

5 Maslanik, J. A. *et al.* A younger, thinner Arctic ice cover: Increased potential for rapid, extensive sea-ice loss. *Geophys Res Lett* **34** (2007). https://doi.org/https://doi.org/10.1029/2007GL032043

6 Meier, W. N. *et al.* NOAA Arctic Report Card 2025 : Sea Ice. (2025). https://doi.org/https://doi.org/10.25923/mmxf-0r86

7 Ding, Q. *et al.* Influence of high-latitude atmospheric circulation changes on summertime Arctic sea ice. *Nature Climate Change* **7**, 289-295 (2017). https://doi.org/10.1038/nclimate3241

8 Polyakov, I. V. *et al.* Greater role for Atlantic inflows on sea-ice loss in the Eurasian Basin of the Arctic Ocean. *Science* **356**, 285-291 (2017). https://doi.org/doi:10.1126/science.aai8204

9 Carmack, E. *et al.* Toward Quantifying the Increasing Role of Oceanic Heat in Sea Ice Loss in the New Arctic. *Bull. Amer. Meteorol. Soc.* **96**, 2079-2105 (2015). https://doi.org/https://doi.org/10.1175/BAMS-D-13-00177.1

10 Blanchard-Wrigglesworth, E., Armour, K. C., Bitz, C. M. & DeWeaver, E. Persistence and Inherent Predictability of Arctic Sea Ice in a GCM Ensemble and Observations. *J Climate* **24**, 231-250 (2011). https://doi.org/https://doi.org/10.1175/2010JCLI3775.1

11 Kwok, R. Arctic sea ice thickness, volume, and multiyear ice coverage: losses and coupled variability (1958–2018). *Environmental Research Letters* **13**, 105005 (2018). https://doi.org/10.1088/1748-9326/aae3ec

12 Francis, J. A. & Wu, B. Why has no new record-minimum Arctic sea-ice extent occurred since September 2012? *Environmental Research Letters* **15**, 114034 (2020). https://doi.org/10.1088/1748-9326/abc047

13 England, M. R., Polvani, L. M., Screen, J. & Chan, A. C. Minimal Arctic Sea Ice Loss in the Last 20 Years, Consistent With Internal Climate Variability. *Geophys Res Lett* **52**, e2025GL116175 (2025). https://doi.org/https://doi.org/10.1029/2025GL116175

14 Ding, Q. *et al.* Fingerprints of internal drivers of Arctic sea ice loss in observations and model simulations. *Nature Geoscience* **12**, 28-33 (2019). https://doi.org/10.1038/s41561-018-0256-8

15 Hanna, E., Cropper, T. E., Hall, R. J. & Cappelen, J. Greenland Blocking Index 1851–2015: a regional climate change signal. *International Journal of Climatology* **36**, 4847-4861 (2016). https://doi.org/https://doi.org/10.1002/joc.4673

16 Wang, S. *et al.* New insight into the influence of the Greenland high on summer Arctic sea ice. *Environmental Research Letters* **17**, 074033 (2022). https://doi.org/10.1088/1748-9326/ac7ac6

17 Wang, S. *et al.* Separation of Atmospheric Circulation Patterns Governing Regional Variability of Arctic Sea Ice in Summer. *Advances in Atmospheric Sciences* **40**, 2344-

2361 (2023). https://doi.org/10.1007/s00376-022-2176-1
18 Huang, Y., Ding, Q., Dong, X., Xi, B. & Baxter, I. Summertime low clouds mediate the impact of the large-scale circulation on Arctic sea ice. *Communications Earth & Environment* **2**, 38 (2021). https://doi.org/10.1038/s43247-021-00114-w
19 Kay, J. E., L'Ecuyer, T., Gettelman, A., Stephens, G. & O'Dell, C. The contribution of cloud and radiation anomalies to the 2007 Arctic sea ice extent minimum. *Geophys Res Lett* **35** (2008). https://doi.org/https://doi.org/10.1029/2008GL033451
20 Huang, Y. *et al.* Thicker Clouds and Accelerated Arctic Sea Ice Decline: The Atmosphere-Sea Ice Interactions in Spring. *Geophys Res Lett* **46**, 6980-6989 (2019). https://doi.org/https://doi.org/10.1029/2019GL082791
21 Kapsch, M.-L., Graversen, R. G. & Tjernström, M. Springtime atmospheric energy transport and the control of Arctic summer sea-ice extent. *Nature Climate Change* **3**, 744-748 (2013). https://doi.org/10.1038/nclimate1884
22 Liu, Y. & Key, J. R. Less winter cloud aids summer 2013 Arctic sea ice return from 2012 minimum. *Environmental Research Letters* **9**, 044002 (2014). https://doi.org/10.1088/1748-9326/9/4/044002
23 Yu, L., Bi, H., Zhong, S., Zhang, P. & Sui, C. Decelerated Arctic Sea ice loss triggered by accelerated North Pacific warming over the past decade. *Communications Earth & Environment* **6**, 922 (2025). https://doi.org/10.1038/s43247-025-02882-1
24 Wang, C. *et al.* Recent slowing of Arctic sea ice melt tied to multidecadal NAO variability. *Nature Communications* **16**, 8504 (2025). https://doi.org/10.1038/s41467-025-63520-0
25 Castruccio, F. S. *et al.* Modulation of Arctic Sea Ice Loss by Atmospheric Teleconnections from Atlantic Multidecadal Variability. *J Climate* **32**, 1419-1441 (2019). https://doi.org/https://doi.org/10.1175/JCLI-D-18-0307.1
26 Zhang, R. Mechanisms for low-frequency variability of summer Arctic sea ice extent. *Proceedings of the National Academy of Sciences* **112**, 4570-4575 (2015). https://doi.org/doi:10.1073/pnas.1422296112
27 Screen, J. A. & Simmonds, I. The central role of diminishing sea ice in recent Arctic temperature amplification. *Nature* **464**, 1334-1337 (2010). https://doi.org/10.1038/nature09051
28 Kay, J. E., Raeder, K., Gettelman, A. & Anderson, J. The Boundary Layer Response to Recent Arctic Sea Ice Loss and Implications for High-Latitude Climate Feedbacks. *J Climate* **24**, 428-447 (2011). https://doi.org/https://doi.org/10.1175/2010JCLI3651.1
29 Overland, J. E. & Wang, M. Large-scale atmospheric circulation changes are associated with the recent loss of Arctic sea ice. *Tellus A* **62**, 1-9 (2010). https://doi.org/https://doi.org/10.1111/j.1600-0870.2009.00421.x
30 Coumou, D., Di Capua, G., Vavrus, S., Wang, L. & Wang, S. The influence of Arctic amplification on mid-latitude summer circulation. *Nature Communications* **9**, 2959 (2018). https://doi.org/10.1038/s41467-018-05256-8
31 Screen, J. A., Simmonds, I., Deser, C. & Tomas, R. The Atmospheric Response to Three Decades of Observed Arctic Sea Ice Loss. *J Climate* **26**, 1230-1248 (2013). https://doi.org/https://doi.org/10.1175/JCLI-D-12-00063.1
32 Vihma, T. Effects of Arctic Sea Ice Decline on Weather and Climate: A Review. *Surveys in Geophysics* **35**, 1175-1214 (2014). https://doi.org/10.1007/s10712-014-9284-0
33 Moore, G. W. K., Schweiger, A., Zhang, J. & Steele, M. Spatiotemporal Variability of Sea Ice in the Arctic's Last Ice Area. *Geophys Res Lett* **46**, 11237-11243 (2019). https://doi.org/https://doi.org/10.1029/2019GL083722
34 Liu, L., Wu, B. & Ding, S. Combined impact of summer NAO and northern Russian

shortwave cloud radiative effect on Eurasian atmospheric circulation. *Environmental Research Letters* **18**, 014015 (2023). https://doi.org/10.1088/1748-9326/acabd9

35 Wang, Z., Zhang, B., Yao, Y. & Zhang, W. GRACE and mass budget method reveal decelerated ice loss in east Greenland in the past decade. *Remote Sensing of Environment* **286**, 113450 (2023). https://doi.org/https://doi.org/10.1016/j.rse.2023.113450

36 van den Broek, D., Urbancic, G. H., Rantanen, M. & Vihma, T. Svalbard's Record-Breaking Arctic Summer 2024: Anomalies Beyond Climatological Warming Trends. *Geophys Res Lett* **52**, e2025GL115015 (2025). https://doi.org/https://doi.org/10.1029/2025GL115015

37 Box, J. E. *et al.* Greenland Ice Sheet Rainfall, Heat and Albedo Feedback Impacts From the Mid-August 2021 Atmospheric River. *Geophys Res Lett* **49**, e2021GL097356 (2022). https://doi.org/https://doi.org/10.1029/2021GL097356

38 Dou, T. *et al.* A key factor initiating surface ablation of Arctic sea ice: earlier and increasing liquid precipitation. *The Cryosphere* **13**, 1233-1246 (2019). https://doi.org/10.5194/tc-13-1233-2019

39 Yang, M., Wang, Z., Walsh, J. E., Doyle, J. D. & Fearon, M. G. Contribution of Arctic Cyclones of Different Origins to Poleward Heat Transport to the Arctic. *J Climate* **38**, 2129-2138 (2025). https://doi.org/https://doi.org/10.1175/JCLI-D-24-0445.1

40 Landrum, L. & Holland, M. M. Extremes become routine in an emerging new Arctic. *Nature Climate Change* **10**, 1108-1115 (2020). https://doi.org/10.1038/s41558-020-0892-z

41 Liu, J. *et al.* Has Arctic Sea Ice Loss Contributed to Increased Surface Melting of the Greenland Ice Sheet? *J Climate* **29**, 3373-3386 (2016). https://doi.org/https://doi.org/10.1175/JCLI-D-15-0391.1

42 Woollings, T. *et al.* Contrasting interannual and multidecadal NAO variability. *Climate Dynamics* **45**, 539-556 (2015). https://doi.org/10.1007/s00382-014-2237-y

43 Peings, Y. & Magnusdottir, G. Forcing of the wintertime atmospheric circulation by the multidecadal fluctuations of the North Atlantic ocean. *Environmental Research Letters* **9**, 034018 (2014). https://doi.org/10.1088/1748-9326/9/3/034018

44 Screen, J. A. & Deser, C. Pacific Ocean Variability Influences the Time of Emergence of a Seasonally Ice-Free Arctic Ocean. *Geophys Res Lett* **46**, 2222-2231 (2019). https://doi.org/https://doi.org/10.1029/2018GL081393

45 Baxter, I. *et al.* How Tropical Pacific Surface Cooling Contributed to Accelerated Sea Ice Melt from 2007 to 2012 as Ice Is Thinned by Anthropogenic Forcing. *J Climate* **32**, 8583-8602 (2019). https://doi.org/https://doi.org/10.1175/JCLI-D-18-0783.1

46 Strong, C. & Rigor, I. G. Arctic marginal ice zone trending wider in summer and narrower in winter. *Geophys Res Lett* **40**, 4864-4868 (2013). https://doi.org/https://doi.org/10.1002/grl.50928

47 Thomson, J. & Rogers, W. E. Swell and sea in the emerging Arctic Ocean. *Geophys Res Lett* **41**, 3136-3140 (2014). https://doi.org/https://doi.org/10.1002/2014GL059983

48 Guemas, V. *et al.* A review on Arctic sea-ice predictability and prediction on seasonal to decadal time-scales. *Quarterly Journal of the Royal Meteorological Society* **142**, 546-561 (2016). https://doi.org/https://doi.org/10.1002/qj.2401

49 Liu, T. *et al.* Teleconnections among tipping elements in the Earth system. *Nature Climate Change* **13**, 67-74 (2023). https://doi.org/10.1038/s41558-022-01558-4

50 Hanna, E., Fettweis, X. & Hall, R. J. Brief communication: Recent changes in summer Greenland blocking captured by none of the CMIP5 models. *The Cryosphere* **12**, 3287-3292 (2018). https://doi.org/10.5194/tc-12-3287-2018

51 Woollings, T. *et al.* Blocking and its Response to Climate Change. *Current Climate*

Change Reports **4**, 287-300 (2018). https://doi.org/10.1007/s40641-018-0108-z

52 Maddison, J. W., Catto, J. L., Hanna, E., Luu, L. N. & Screen, J. A. Missing Increase in Summer Greenland Blocking in Climate Models. *Geophys Res Lett* **51**, e2024GL108505 (2024). https://doi.org/https://doi.org/10.1029/2024GL108505

53 Davini, P. & D'Andrea, F. From CMIP3 to CMIP6: Northern Hemisphere Atmospheric Blocking Simulation in Present and Future Climate. *J Climate* **33**, 10021-10038 (2020). https://doi.org/https://doi.org/10.1175/JCLI-D-19-0862.1

54 Comiso, J. C. *et al.* Positive Trend in the Antarctic Sea Ice Cover and Associated Changes in Surface Temperature. *J Climate* **30**, 2251-2267 (2017). https://doi.org/https://doi.org/10.1175/JCLI-D-16-0408.1

55 Zhang, J. & Rothrock, D. A. Modeling Global Sea Ice with a Thickness and Enthalpy Distribution Model in Generalized Curvilinear Coordinates. *Monthly Weather Review* **131**, 845-861 (2003). https://doi.org/https://doi.org/10.1175/1520-0493(2003)131<0845:MGSIWA>2.0.CO;2

56 Schweiger, A. *et al.* Uncertainty in modeled Arctic sea ice volume. *Journal of Geophysical Research: Oceans* **116** (2011). https://doi.org/https://doi.org/10.1029/2011JC007084

57 Tschudi, M., Meier, W. N., Stewart, J. S., Fowler, C. & Maslanik, J. (NASA National Snow and Ice Data Center Distributed Active Archive Center, Boulder, Colorado USA, 2025).

58 Hersbach, H. *et al.* The ERA5 global reanalysis. *Quarterly Journal of the Royal Meteorological Society* **146**, 1999-2049 (2020). https://doi.org/https://doi.org/10.1002/qj.3803

59 Kato, S. *et al.* Surface Irradiances of Edition 4.0 Clouds and the Earth's Radiant Energy System (CERES) Energy Balanced and Filled (EBAF) Data Product. *J Climate* **31**, 4501-4527 (2018). https://doi.org/https://doi.org/10.1175/JCLI-D-17-0523.1

60 Danabasoglu, G. *et al.* The Community Earth System Model Version 2 (CESM2). *Journal of Advances in Modeling Earth Systems* **12**, e2019MS001916 (2020). https://doi.org/https://doi.org/10.1029/2019MS001916

61 Rodgers, K. B. *et al.* Ubiquity of human-induced changes in climate variability. *Earth Syst. Dynam.* **12**, 1393-1411 (2021). https://doi.org/10.5194/esd-12-1393-2021

62 Wu, B., Wang, J. & Walsh, J. E. Dipole Anomaly in the Winter Arctic Atmosphere and Its Association with Sea Ice Motion. *J Climate* **19**, 210-225 (2006). https://doi.org/10.1175/jcli3619.1

63 Hobday, A. J. *et al.* A hierarchical approach to defining marine heatwaves. *Progress in Oceanography* **141**, 227-238 (2016). https://doi.org/https://doi.org/10.1016/j.pocean.2015.12.014

64 Zhang, K. *et al.* Global prevalence of compound heatwaves from 1980 to 2022. *Advances in Climate Change Research* **16**, 565-575 (2025). https://doi.org/https://doi.org/10.1016/j.accre.2025.04.010

Supplementary Files

This is a list of supplementary files associated with this preprint. Click to download.

- SupplementaryInformationGHSIE.docx